Rotating Live Mammalian Cells Free in Media

Using Spatial Light Modulator (SLM)-Generated Optical Tweezers

by

Samantha W. Chan

A Thesis Presented in Partial Fulfillment
of the Requirements for the Degree
Master of Science

Approved June 2013 by the
Graduate Supervisory Committee:

Deirdre R. Meldrum, Chair
Jeffrey A. Kleim
Roger H. Johnson
Laimonas Kelbauskas

ARIZONA STATE UNIVERISTY

August 2013

ABSTRACT

In the frenzy of next generation genetic sequencing and proteomics, single-cell level analysis has begun to find its place in the crux of personalized medicine and cancer research. Single live cell 3D imaging technology is one of the most useful ways of providing spatial and morphological details inside living single cells. It provides a window to uncover the mysteries of protein structure and folding, as well as genetic expression over time, which will tremendously improve the state of the fields of biophysics and biomedical research. This thesis project specifically demonstrates a method for live single cell rotation required to image them in the single live cell CT imaging platform. The method of rotation proposed in this thesis uses dynamic optical traps generated by a phase-only spatial light modulator (SLM) to exert torque on a single mammalian cell. Laser patterns carrying the holographic information of the traps are delivered from the SLM through a transformation telescope into the objective lens and onto its focal plane to produce the desired optical trap “image”. The phase information in the laser patterns being delivered are continuously altered by the SLM such that the structure of the wavefront produces two foci at opposite edges of the cell of interest that each moves along the circumference of the cell in opposite axial directions. Momentum generated by the motion of the foci exerts a torque on the cell, causing it to rotate. The viability of this method was demonstrated experimentally. Software was written using LabVIEW to control the display panel of the SLM.

TABLE OF CONTENTS

Page

CHAPTER Page

LIST OF FIGURES

Figure Page

Figure Page

Figure Page

LIST OF TABLES

Table Page

Chapter 1 Introduction to Single Live Cell Computed Tomography

1.1 Introduction

For decades, scientists have been working to improve the resolution and accuracy of micro-imaging techniques. The knowledge available about the biology of cells today would not have come so far without the advancement in microscopy. Today, engineers strive to continue to push the limits of resolution and methods of imaging at the single cell level, as there remain many mysteries to be solved that surrounds the biology of an individual cell. Clear understanding of cell morphology and its dynamics can shed light on many diseases, and open doors to new and better treatments. Three dimensional (3D) single cell imaging is gaining a lot of attention from the medical and biological community, because the ability to view small structures within the cell in three dimensions can provide spatiotemporal information about how particulates within the cell interact with each other. This structural and interaction information of proteins and molecules in the cell is often the key to important insights, breakthroughs or cures, but is difficult to achieve with mere two dimensional imaging. Much research have focused on devising techniques to analyze single cells on microscale chips (Lidstrom and Meldrum 2003), and many more have already proven single cell 3D imaging possible and insightful in diagnosis and understanding of diseases such as cancer (Nandakumar et al. 2012; Nandakumar, Holl, and Meldrum 2008; Ashcroft et al. 2011).

The main motivation for this thesis project is to develop a cell rotation system that can be incorporated into the much larger scaled single live cell optical computed tomography (CT) imaging system. This project is therefore tailored towards the typical demands of a single cell CT system.

Single cell CT imaging is not so different from CT scans commonly done on patients in a hospital. Human CT imaging usually involves the patient lying in place while an X-ray source and a detector rotate around the imaging area of interest in full circle. These X-ray projections can then be combined through algorithms such as Radon transforms to reconstruct a 3D-image of internal organs, so as to assist physicians in obtaining a more accurately diagnosis of the patient. The same principle of passing waves through the object of interest and taking projections can be applied in single cell optical CT, but instead of having the microscope rotate around the cell, the cell will rotate in a constant and fixed field of light. Single cell optical CT technology was pioneered by VisionGate (Fauver et al. 2005). Cells are fixed in a gel that is then delivered through a capillary tube over a microscope objective lens. Once a single cell of interest is chosen for imaging, the capillary tube will rotate while light is passed perpendicularly through the capillary to take projection images of the cell at many different angles as it rotates. The projected images are collected, analyzed, and processed through software, and then combined through complex algorithms to reconstruct 3D images of the cell, revealing its volumetric structures. CT of cells using light will typically have a resolution of approximately 0.35μm (Nandakumar et al. 2011), which is sufficient for a clear 3D view of intracellular structures such as chromosomes, mitochondria, and endoplasmic reticulum. Because the cell is a 3D structure, there are obvious advantages of imaging in 3D as opposed to 2D space. Some of these advantages include better understanding of binding structures and properties of the cell, and much improved insight to the spatial distribution of intercellular organelles and structures. For these reasons, the single cell CT technology can also become a useful diagnostic tool for cancer or other diseases.

One major drawback of VisionGate's cell CT system is that cells must be fixed and packed in a gel medium that is toxic and invasive, which means that the cells cannot be imaged in their natural, live state. This introduces much uncertainty to researchers who would like to know the truth about the living state of a cell. The ability to image live cells also opens a window for observing dynamic events in the cell, as well as effects of drugs or other substances in a cell over time. This thesis project presents a method to rotate live cells non-invasively, which brings live cell tomography one step closer to realization.

There are some major requirements the cell rotation method must meet in order to adopt it into current live cell CT technologies. First, the method of rotation must be minimally invasive to the cell, such as to keep disruption to the cell and its environment to a minimum. Secondly, rotation of the cell must be stable and at a constant rate, so as to increase the accuracy of reconstruction. Lastly, and most importantly, the cell must be rotated about an axis perpendicular to the optical axis of the imaging system. This is essential for 3D reconstruction of the cell. It is relatively trivial to rotate a cell around the axis of the imaging objective lens, but the projections taken from the cell will be completely useless for 3D reconstruction, since only one side of the cell is constantly being exposed to the imaging lens. Image projections must be taken from as many angles of the cell as possible. It would also be considerably more computationally efficient to reconstruct the cell if the cell were rotating at a fixed perpendicular axis, thus once again stressing the importance of stability.

Optical cell rotation is only one of many methods that can be adopted by the single live cell CT system. Other modes of rotation include the use of microfluidics

(Leung et al. 2012), microvortices (Myers 2012; Parkin et al. 2007), and the use of dielectrophoretic forces in an electrocage system (Elango 2012; Fuhr et al. 1992; Schnelle et al. 2000; Le Saux et al. 2009). At their current stages of development, it is difficult to distinguish the best method to be adopted into the live cell CT system, as they all possess unique advantages as well as limitations. One microvorti-based method uses microfabrication techniques to create channels with trapezoidal chambers, where cells will flow over and become trapped. The cell will then rotate due to microfluidic forces, where the rate of rotation can be controlled by the flow rate as well as chamber dimensions. The disadvantage of this method is that there is very little selectivity of the cell of interest; whether the cell trapped in the chamber is desirable or not is left completely to chance. Although this is easily remedied by using optical tweezers, it adds unwanted complexity to the already intricate microfluidic system, making the microvortex rotation a cumbersome method to implement. Electrorotation is the most mature of the three methods of rotation, as there is extensive literature on the characterization and microfabrication techniques for the electrocage system. The electrorotation method uses microfabrication techniques to build electrodes that are arranged in such a way that a small chamber is created. Alternating electric fields with appropriate phase delays are applied to the different electrodes to generate dielectrophoretic force to induce cell rotation. This technique shows great promise, such that with the help of optical tweezers, cells can be selected and removed from the chamber for further analysis. Though this is the case, the effect of high frequency electromagnetic fluctuations on the cell function is still controversial (Gray et al. 2004).

The optical cell rotation proposed in this thesis project is a method that uses laser light with a biologically non-invasive wavelength of 1064 nm to rotate cells. From the discussion of optical tweezers in Chapter 2, a focused Gaussian laser beam is able to trap a cell into its focus spot, giving it 3D control over the position of a cell. This entails that optical tweezers with sufficient power should have the capability to rotate a live cell about any axis. The hypothesis in this thesis is that by applying a focused beam on either side of a cell, and maneuvering it up and down the axial axis with equal and opposite forces continuously, the sides of the cell will be trapped by the optical tweezers, and the axial oscillations of the tweezers will exert enough torque to initiate cell rotation about the axis perpendicular to the optical axis of the imaging objective lens.

1.2 State of the Art

Prior research has already demonstrated 3D optical rotation and orientation of structures. However, to date this has only been reported on microparticles (Sheu et al. 2010; Mohanty, Dasgupta, and Gupta 2005), bacteria cells (Carmon and Feingold 2011; Banerjee et al. 2011) or small mammalian cells, such as the red blood cells (Sato, Ishigure, and Inaba 1991; Kreysing et al. 2008; Dasgupta et al. 2011). Bacteria cells are relatively easy to handle three-dimensionally with optical tweezers. The mass of a bacteria cell is much smaller than a mammalian cell; the size of a mammalian cell can range from about 15μm to 30μm in diameter (Gregory 2000), while that of bacteria cells are usually only about 2μm to 5μm (Bronk, Merwe, and Stanley 1992). The amount of power per trap that would be required to manipulate bacteria cells is orders of magnitude less than that would be for a mammalian cell. This makes it simple to trap arrays of bacteria cells simultaneously, but very challenging to do the same with mammalian cells.

Asymmetric cells are also relatively easier to trap, because their asymmetry allows them to orient themselves with the beam due to the random distribution of organelles and density within the cell (Perney et al. 2012). Mammalian cells are usually spherical in suspension, thus have relatively symmetric dimensions as compared with some bacteria cells that can be very asymmetric as they vary in shapes and sizes.

Many have demonstrated optical orientation and rotation of particles using Laguerre-Gaussian (LG) mode beams. LG beams have an indigenous orbital angular momentum, thus it naturally became the most popular light mode to use for optical rotation and orientation. Dasgupta et al. demonstrated full 3D orientations and rotation of red blood cells using LG trapping beams generated by a SLM (Dasgupta et al. 2011). Another group used pure Gaussian mode beams without the use of a SLM, and created dual mode split beam optical tweezers by passing a single mode beam through a slit. This enabled them to rotate red blood cells about the optical axis (Sheu et al. 2010), but much modification of this set-up is needed to rotate cells about the perpendicular axis of the optical axis. One group used the SLM to generate separate LG mode optical traps that were then guided separately into two different high power lenses to create counter propagating beams (Čižmár et al. 2011). These counter-propagating beams held the particle in suspension, and together rotated the particle with the inherent orbital angular momentum of the LG mode beam. Still, other modes of optical tweezers have been used in a similar way, such as the elliptical mode (Mohanty, Dasgupta, and Gupta 2005). There is also a group that has demonstrated optical rotation by delivering counter propagating beams through single and dual mode optical fibers using fiber splicing techniques (Kreysing et al. 2008). This seems to be the most promising method of

rotation to adopt into the live cell CT system. It not only shows stability and high controllability in rate of rotation, it is possible to trap cells larger than red blood cells. Although this is the case, the power needed may overcome the tolerance of the optical fiber, and as a result may cause distortion to the beam profile or simply break the fiber. No pure optical rotation has been demonstrated on mammalian cells larger than a red blood cell yet.

1.3 Discussion

This chapter provides the motivation for this thesis, and thoroughly reviews the current state of single live cell CT imaging and single cell rotation technologies. The beginning of the chapter emphasizes the importance of being able to examine cells in 3D space, and that single live cell CT technology can push the envelope forward to potentially answer questions about the natural state of microorganisms in a way current technologies struggle to do. Common strategies being used in the optical cell manipulation community, and the pros and cons of each method are briefly discussed, and the reasons behind why the optical cell rotation method is desirable for single cell CT were explained. Current state-of-the-art single cell CT technology belongs to VisionGate. The project in this thesis directly addresses the limitation in VisionGate's platform, where it is unable to rotate and image live cells. The advantages of imaging live cells as opposed to imaging fixed cells were also discussed in this chapter. The following chapter will provide the basic theories behind single cell rotation using coherent laser light and Fourier optics.

The core contributions of the author of this thesis include designing the method of optical cell rotation using the SLM, writing LabVIEW control software to generate and

display holograms on the SLM by implementing algorithms in current literature, and characterizing and optimizing cell rotation.

Chapter 2 Introduction to Optical Cell Manipulation

2.1 Introduction

Optical micro manipulation has come a long way since 1970, when Ashkin first demonstrated that the radiation power of tightly focused laser beams can accelerate and trap microscopic masses (Ashkin 1970). It was not until 1986 when Ashkin first demonstrated the first truly 3D optical manipulation, which not only accelerated micro particles using a tightly focused laser beam, but also confined individual particles three-dimensionally without the need of external forces (Ashkin et al. 1986). This "single-beam gradient force optical trap", later simply known as "optical tweezers", opened the world of biological research to much wider possibilities on the single-cell level, protein level, genetic level, and even atomic level. The importance of the discovery of optical micro manipulation resonated when a Nobel Prize was awarded to Steven Chu "for [developing] methods to cool and trap atoms with laser light" (Chu et al. 1986). In the early 2000s, scientists and engineers began to realize that holographic beam-shaping can be used for extending the utilities of optical tweezers. By structuring the wavefront of a laser beam using computer-generated diffractive optical elements (a.k.a. holograms), multiple optical traps can be delivered through a single objective lens, and consequently, multiple particles can be manipulated simultaneously. Holographic optical tweezers have now become the preferred method for most applications that involve simultaneous control over multiple particles, and remain the unrivaled option when it comes to full 3D manipulation of asymmetric particles.

The motivation for this thesis is to provide a means for mammalian cell rotation under the microscope for optical live cell tomography. Holographic optical tweezers

generated by a computer-controlled spatial light modulator (SLM) will be the main tool for cell rotation in this thesis, but it is only one of many methods for micro-particle manipulation. Nonetheless, the simplicity and elegance that holographic optical tweezers offer in micro manipulation is truly irrefutable.

Chapter 2 of this thesis provides a brief overview of the basic principles behind holographic optical tweezers. Chapter 3 discusses the methods of optical cell rotation on the optical set-up level. Chapter 4 presents the computational algorithms and methods used for creating the holograms necessary for generating the optical tweezers discussed in Chapter 3. Results, characterization and optimization of the holographic optical cell rotation are presented in Chapter 5. The thesis will conclude with an overall summary and a discussion on future prospects of this project in Chapter 6.

2.2 Theory

To effectively structure light using holography, one must have a good understanding of the properties of light. This section of the thesis serves to provide a background on the theories in optics and photonics applied in this particular project, so as to provide the reader with the basic tools to perform holographic optical micromanipulation.

2.2.1 Light and Lasers

The nature of light was long a controversial subject as physicists debated whether light was a wave or made up of discrete particles. It was only until the early twentieth century that physicists began to understand the dual nature of light, and came to a consensus that light is both wave and particle. Owing mainly to the genius of James Clerk Maxwell (1831 – 1879), it is now known that visible light is simply one form of

electromagnetic energy – a small subsection of a larger spectrum of electromagnetic waves, which spans from radio waves to infrared radiation, the visible spectrum of light, ultraviolet radiation, x-rays, and gamma radiation. Quantum theory of light, pioneered by Planck, Einstein, and Bohr, later proved that electromagnetic energy is quantized; which means light can only be imparted or taken from the electromagnetic field in discrete amounts called photons. It is thus that some phenomena, such as interference, exhibits wave characteristics of light, while other phenomena, such as the photoelectric effect, exhibits the particle properties of light. The reflection and refraction property of light as a wave, and the linear momentum of light as a particle are what give optical tweezers their remarkable ability to trap particles. The way these two properties work together to create an optical trap will be discussed in the following section.

Lasers (Light Amplified by Stimulated Emission of Radiation) play a vital role in optical micromanipulation applications. Light emitted from lasers is monochromatic, coherent, and directional. A laser system contains a lasing medium (or gain medium) and an excitation energy source. The lasing medium is commonly a form of gas or crystals, which harbors the atoms responsible for energy absorption and emission. When a laser is activated, a large population of atoms or molecules is excited and reaches a higher energy state. In other words, the laser reaches a certain level of population inversion. As they return to the ground energy level, a large proportion of excited atoms/molecules can then emit photons at a high enough flux to begin the lasing process. Figure 1 provides a schematic of stimulated emission in lasers. Intense light or electric discharges can be used to “pump” the lasing medium, so that the atoms in the medium enter the initial excited state (usually two or three levels above the ground state). This will produce a high

proportion of excited atoms relative to ground state atoms, i.e. high population inversion. When an atom in a lasing medium is at a high energy state, it releases energy in the form of photons to reduce back to its ground state. An emitted photon will have a very specific wavelength that is dependent on the state of the electron's energy when the photon is released. Two identical atoms with electrons at the same energy level will release photons of identical wavelengths. When population inversion reaches a sufficient level, optical amplification can take place. As an atom in its excited state spontaneously emits a photon at a certain wavelength and phase, it may encounter another electron that is at the same excited state. The first photon can stimulate (induce) atomic emission such that the subsequent emitted photon from the second atom resonates with the first, and will thus travel in the direction as the incoming photon. This is called stimulated emission.

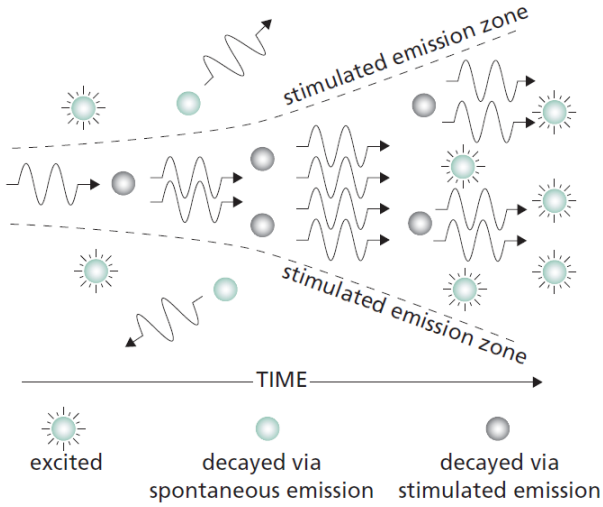

Figure 1. Amplification via stimulated emission in laser system (Herd, Dover, and Arndt 1997)

A laser system also has a pair of mirrors, which plays a very crucial role in laser emission. The mirrors complete and sustain the optical amplification process. A mirror is situated on opposite ends of the laser tube containing the lasing medium. When

stimulated emission takes place in the medium, the photons emitted will travel to one of the mirrors and are reflected back through the excited atoms in the lasing medium, which stimulate more photon emission on its way to the other mirror. The photons that reach the second mirror are in turn reflected repeatedly in the same way, all the while exciting more electrons and emitting more photons until the amount of photons emitted reaches a saturated equilibrium state that is dependent on the input power of the laser.

The laser used in this thesis project is a diode-pumped solid-state (DPSS) Nd:YAG (neodymium-doped yttrium aluminum garnet; Nd:$Y_3Al_5O_{12}$) laser. For this particular type of lasing medium, the characteristic wavelength of photons emitted is at the near infrared spectrum of 1064nm. Nd:YAG is typically pumped with incandescent tungsten lamps, and is one of the most efficient types of lasers, having the capability to emit continuous waves of light necessary for optical tweezing applications. Other types of lasers include but are not restricted to gas lasers, chemical lasers, dye lasers, metal-vapor lasers, semi-conductor lasers, and Raman lasers, all of which are beyond the scope of this thesis, and thus will not be discussed here.

2.2.2 Basic Principles of Optical Tweezers

The coherence and directional properties of lasers are important factors for optical trapping. The way that light interacts with particles can be differentiated into two regimes: the Rayleigh scattering regime and the Mie regime. In the Rayleigh regime, the particle that interacts with the incoming light is much smaller than the wavelength of the light, and is usually studied using the Electric Dipole approximation; in the Mie regime, the particle that interacts with the light is much larger (diameter approximately 4λ) than the wavelength of the light, and can instead be studied using the geometric Ray Optics

approach. Figure 2 provides an illustration that distinguishes the two regimes. In this thesis, a 1064nm wavelength laser is used to optically rotate mammalian cells with diameters that range anywhere between 15µm to 25µm. This study therefore lies in the Mie regime. In this case, optical tweezing can more simply be understood using geometric ray optics analysis.

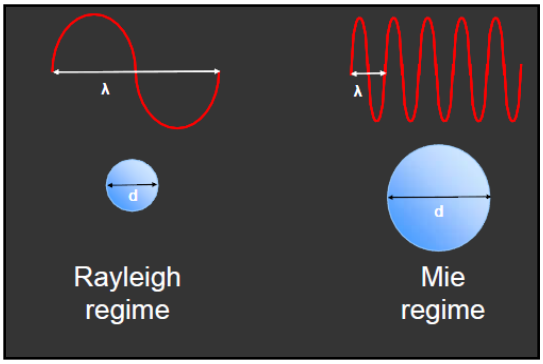

Figure 2. The particle size relative to the wavelength of light determines the regime of optical analysis (EINST Technology Pte Ltd 2003)

Ray optics analysis basically involves the tracing of the incident light path through the dielectric (i.e. transparent) microsphere of interest. This allows computation of the reflection and refraction angles of those rays as well as the resultant forces imparted on the particle due to the transfer of linear momentum from light to the particle. From basic optical physics, the speed of light is dependent on the refractive index of the medium in which it is traveling through. When an incident light travels from a medium of refractive index n_1 to another medium with refractive index n_2, the speed of light changes at the interface, resulting in a "bending" of light, or refraction, at an angle θ_2 dependent on the angle of incidence θ_1, and the refractive indices n_1 and n_2. The relationship can be described using Snell's Law:

$$n_1 \sin\theta_1 = n_2 \sin\theta_2$$

In general, stable optical trapping requires that the particle has a higher index of refraction than its outer medium by a ratio ranging from of about 1.1 to 1.2. As pointed out later, the angle of incidence as well as the distribution of the intensity of the beam profile plays a significant role in the stability of the optical trap.

Since light has linear momentum, when light hits the surface of a dielectric particle, a transfer of momentum occurs, and the particle experiences a scattering force along the propagation direction of the light path. This scattering force is responsible for one of the two force components of the optical trap F_s. As light enters a dielectric particle, refraction occurs, and light changes direction at the interface. This change of direction causes a change in linear momentum through the particle. By Newton's second law of motion and conservation of momentum, a force of equal and opposite direction will be exerted onto the particle. This creates the second force component of the optical trap, the gradient force F_g, which is perpendicular to the scattering force F_s.

The strength and stability of an optical trap is dependent on the total effective F_s and F_g. As mentioned earlier, the distribution of the incident light intensity can greatly influence the efficacy of an optical trap. Generally, a Gaussian beam, or a variation of a Gaussian beam, is used for optical trapping. The reason behind this can be explained using the concepts of ray optics discussed previously. When a dielectric particle is exposed to an intensity gradient, the particle will move towards the region of highest intensity, because the resultant gradient force from the refraction of high intensity light will overcome the gradient force generated from the refraction of lower intensity light, creating a net gradient force exerted in the direction of the highest light intensity. When a

Gaussian beam is used, the particle will be trapped towards the center of the beam with highest intensity, thus restricting the lateral displacement of the cell.

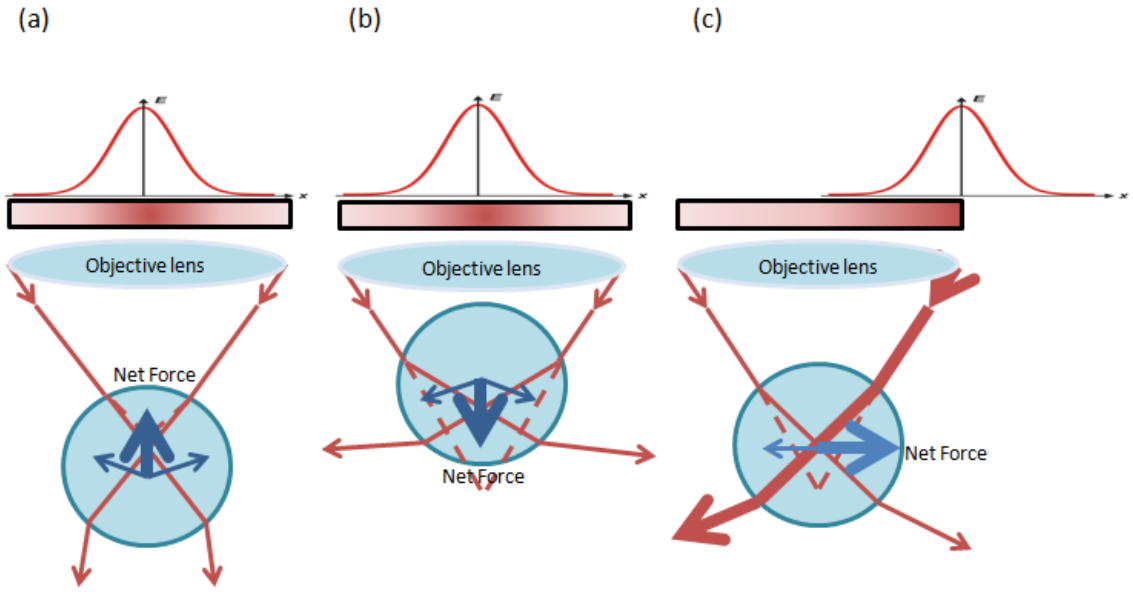

Figure 3. Gradient and scattering effect of optical tweezers: a) and b) a net resultant force draws the dielectric sphere towards the laser focus where beam intensity is highest; c) resultant gradient force is generated under an intensity gradient, drawing the sphere towards the region of highest intensity

Angle of incidence is also a key factor that controls optical trapping performance, and is what gives optical traps control over a third dimension, as it adds an axial component to optical trapping. In order to create a steep angle upon entering the particle, a focused beam is used. A beam can be focused by delivering the collimated laser light onto the specimen using an objective lens. An important characteristic to consider in an objective lens is the numerical aperture (NA) of the lens. The NA is a dimensionless number that characterizes the range of angles over which the objective lens and pass light

through. NA is dependent on the index of refraction, n, of the lens, and the angle of incidence, θ:

$$NA = n \sin \theta$$

The higher the NA of the objective lens, the larger the angle of incidence, the more stable the trap. In addition to the gradient force that is produced by the Gaussian intensity distribution, a net axial gradient force is also exerted on the particle. In order to create a stable trap, a delicate balance between the gradient force and the scattering force must be met. A beam focused with a high NA lens enters the particle at a large angle. This means the center of the particle will be trapped at the focus point with a minimized scattering force, which can be easily balanced by the resultant axial gradient force created by refraction of light as it enters and leaves the cell. If the angle of incident is too low, the scattering force will dominate, pushing the particle away from the focus point. Figure 3 shows a ray force diagram of a dielectric sphere under different intensity gradients and different positions along the optical axis of the objective lens on the bead. It illustrates the relationship between angle and intensity with resultant trapping force. Together, the angle of incidence and intensity gradient make 3D optical micromanipulation possible.

2.2.3 Fourier Optics

Fourier optics is used in many optical information processing applications, and is a subject that is highly relevant to the field of holography, but it is so vastly complex that it is impossible to do the subject justice within the scope of this thesis. The reason for Fourier optics' unassailable importance in the study of holography all comes down to the special Fourier transforming properties of a simple lens. Since this thesis project

exclusively uses aspheric (positive or convergent) lenses, as the main optical element, only the Fourier optics of aspheric lenses will be discussed here.

The Fourier transformation is a fundamental method of reversibly transforming data to and from the spatial domain and the frequency domain. The aspheric lens has a remarkable ability to Fourier transform or inverse-Fourier transform incoming light. While Fourier theory is more commonly explained through mathematics, for the purposes of this thesis, it will be simpler and more intuitive to understand the Fourier transformation properties of a simple lens through ray optics. Nonetheless, full mathematical derivations of Fourier optics equations can be found in Joseph W. Goodman's book entitled "Introduction to Fourier Optics."

It is known that light is both wave and particle, and that waves have phase. Light also has phase, but since light is also a particle, how is phase imparted on individual photons? A common misconception is that each individual photon constantly changes phase over time like the hands of a clock that spins at a certain frequency. In reality, because photons are traveling at the speed of light, by the laws of relativity, it makes no sense for a photon's phase to change with time! Each individual photon has its own individual phase. A characteristic undulating change in phase of coherent light is observed, because the photons of a plane wave are organized in a way that all the photons at a given plane of the beam share the same phase, and each subsequent wavefront is slightly phase-delayed from the previous one, much like Figure 4 describes.

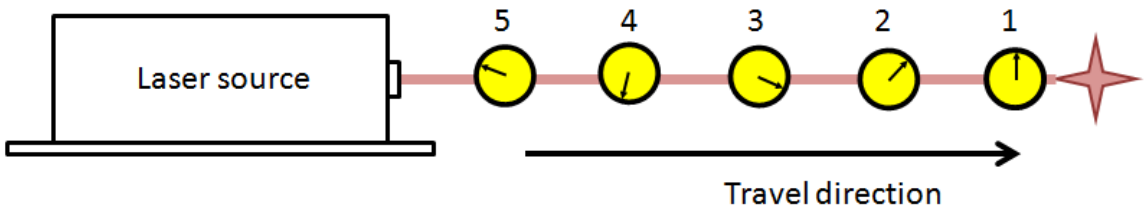

Figure 4. Phase of a laser beam

When laser light passes through a piece of glass with uniform thickness, the beam output will also be coherent and collimated. This is because even if the light had been entering at an angle, each photon at the wavefront is refracted at an identical angle, and travels through a layer of glass of identical thickness, and thus is slowed down at the exact same rate and leaves the glass at the exact same moment, leaving the beam in sync as it were before entering the glass. On the other hand, when coherent light passes through a non-uniformly thick piece of glass, such as one with a curved surface (i.e. a lens), the wavefront of the output light will no longer retain the same profile as the input light. In Figure 5a, Light from the periphery of the lens enters the glass at position 1 and reaches position A via a much shorter distance than it reaches position E. The phase of the photon that reaches position E from position 1 is therefore much delayed than the photon that reaches position A at any given time point. Like a vector, phase is illustrated as arrows that can span 360^{o}, and the intensity of the light is represented by the length of the arrow. Figure 5b roughly describes the magnitude and phase at each position A through E as the result of photons arriving from the respective positions 1 through 5 from Figure 5a.

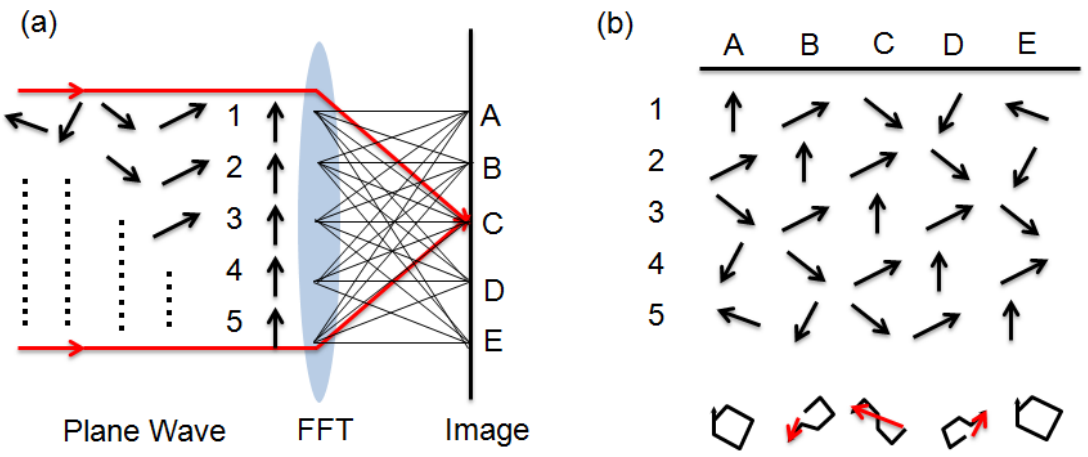

Figure 5. a) Ray path of coherent light through a lens; b) Resultant magnitude and phase of transformed light

Like any wave, light can undergo constructive and destructive interference. Since the properties of light can be described as a vector, where both phase and magnitude is represented by the direction as well as the length of the "arrow", these light vectors are additive. When the vectors are added up at each position of the image plane, the resultant vector contains information of both magnitude and phase of light at that position. Position A decidedly has zero resultant light intensity, because the phase vectors that arrive at position A add up to have equal magnitude and opposite phase, hence canceling each other out and resulting with no light. On the other hand, light that arrives at position C is collectively more constructive, as most of the photons there arrive to share similar phase, resulting in an additive magnitude. The periphery of the image plane therefore has little to no light intensity, while the center of the image plane has the highest intensity. The distribution of the beam becomes Gaussian, and depending on the power of the lens, the sharpness of the resultant Gaussian beam may vary. The lens acts as a function, and the resultant light is said to be "transformed". In Fourier optics terms, when light of a certain

wavelength passes through an aspheric lens, a sharp focus point, or a delta function is produced, thus showing characteristics of a Fourier transformation. The next section shows that the simple aspheric lens is capable of much more complex Fourier transformations than simply producing a single delta function.

2.2.4 Spatial Light Modulators

The spatial light modulator (SLM) is a device that has a reflective panel that can alter the wavefront of an incident beam of light. Most SLMs are only able to modulate either intensity or phase of light, but SLMs have advanced to a level where some are able to modulate both intensity and phase of light simultaneously. SLMs are most widely found in overhead projectors, and are also used extensively for holographic data storage. In addition, SLMs often find applications in the scientific research community, such as in optical computing and holographic optical tweezers.

There are two basic types of SLMs: the optically addressed SLM (OASLM) and the electrically addressed SLM (EASLM). The OASLM is controlled by “incoherent” optical input signals, which is detected by a photo-detector that is able to detect charge distribution over the panel. This charge distribution affects the SLM, and so changes the amplitude or phase of the reflected coherent light, as shown in Figure 6. The EASLM, however, is far more versatile in its applications, and is much preferred for fields outside of coherent optical processing due to the fact that it can be electrically controlled. The EASLMs are characterized by the fact that the light is modulated in pixels, so image resolution is dependent on the pixel size of the device. The SLM used in this project is a Liquid Crystal on Silicon (LCoS) EASLM, and thus from this point onwards, the usage of the term “SLM” will automatically imply the EASLM unless otherwise specified.

There are several main types of developments of the SLM technology. They include liquid crystal (LC) modulators, magneto-optic modulators, deformable mirror, and multiple quantum well technologies. The type used for this project is the LC modulator. Although it suffers in speed compared to other options, it is easily implemented in all applications that call for a SLM, including holographic optical tweezers.

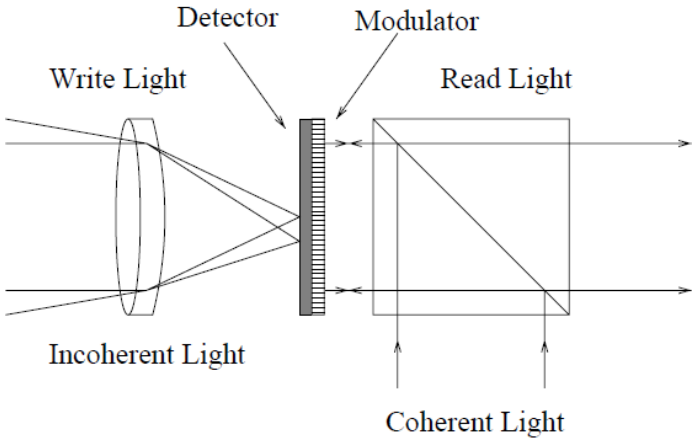

Figure 6. Optically Addressed SLM (Hossack 2012)

There are two main types of liquid crystal modulator EASLMs: Transmissive LC panels, and the LCoS mentioned previously. The transmissive LC panels have liquid crystals between two glass sheets, with control circuitry added with thin film transistors that turn pixels on and off. Each pixel is addressed independently; altering the time each pixel is on controls the grayscale of the image, while arrays of color filters can be placed on top of the device to display images in color. This type of LC display is excellent for image display and projection system. It is commonly found in computer monitors, television sets and projection heads. However, they have large pixels with small fill-factor (or dead space), and are typically not very flat, which becomes non-ideal for coherent optics. The LCoS operates by reflecting coherent light and altering its wavefront

by controlling the voltage supplied by mirrors on a silicon chip. A schematic of the LCoS can be found in Figure 7. The silicon backplane is essentially a chip with reflective mirrors. These individual mirrors can be addressed with a voltage, which in turn "switches on" the LC above the mirror. This change in charge temporarily alters the optical properties of the LC above the mirror, such that when an incident beam of light reaches the LC of a particular pixel, it will independently change the phase of the incoming light. These LCoS devices are much smaller and have much higher resolution than that of the transmissive LC panels. They are also very easy to interface with because they are compatible with standard TTL electronics. For the above reasons, the LCoS naturally became the device of choice for this project.

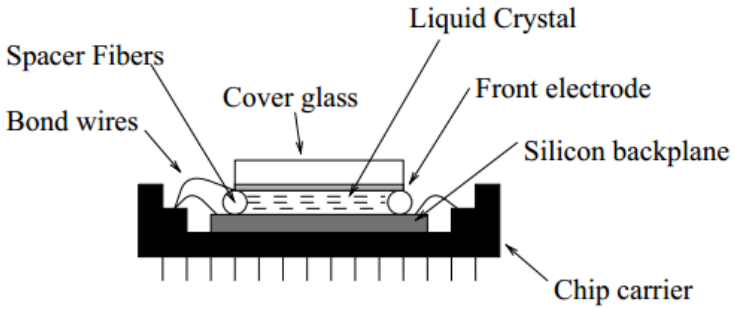

Figure 7. LCoS Electrically Addressed Spatial Light Modulator (Hossack 2012)

2.2.5 Holograms

There remains the question as to what is to be displayed onto the SLM, and how it should be interpreted. It is known that a simple convex lens Fourier transforms light. To produce a desired image through a lens, some type of light pattern must pass through the lens where it will then be Fourier transformed to produce this desired image. That means that the light at the pre-transformed state must contain the inverse-Fourier transform of the desired image. The role of the SLM is to produce an inverse-Fourier transformation

light pattern of the desired image from a coherent light source, and pass this inverse-Fourier transformed wavefront through a lens so that it can be Fourier transformed into the desired image. This inverse-Fourier transformed image that is being displayed on the SLM is called a hologram. The hologram can be generated using computer algorithms. These computer algorithms can be iterative or analytical. Holograms, when displayed on a regular computer monitor, is usually in grayscale (0 to 255); when displayed on the SLM, these grayscale values become voltage signals, and are sent to their respective pixel on the SLM where they produce complex phase shifts ranging from 0 to 2π. The hologram is able to address each pixel on the SLM with a voltage that can alter the optical properties of the LC. This alteration can impart the desired amount of phase shift onto the incoming light before it is reflected. There are numerous methods of generating holograms depending on the application. Software was written in LabVIEW (National Instruments LabVIEW 2010 SP1) to generate holograms for the optical tweezers used in this project. The methods and algorithms used for generating holograms in this project will be discussed in Chapter 4.

2.3 Aberrations

The structure of light is very sensitive to the optical properties of the medium through which it travels, and thus any flaws in the optical set-up can cause serious distortions, or aberrations on the resultant image. There are many types of aberrations that can occur depending on the optical set-up, and they usually occur in combinations rather than alone. This thesis discusses only the types of aberrations for monochromatic light. These aberrations include spherical aberration, astigmatism, coma, and distortion. Ray tracing methods can be used to understand aberrations.

2.3.1 Spherical Aberration

Spherical aberration is perhaps the most prominent type of aberration, and perhaps the most difficult type of aberration to correct. An aberration-free lens should be able to focus incoming collimated light as shown in the upper image on Figure 8. All the rays should pass through the focal point F". However, this is an idealized schematic of light focusing through a lens. In fact, the lower image shows a situation that is more typically encountered with aspheric lenses. The farther from the optical axis the rays enter the lens, the closer to the lens the rays "focus" or intercept the optical axis. The distance between the intercept of the rays originating nearest to the optical axis (i.e. paraxial rays) and that from the periphery of the lens (i.e. marginal rays) is called longitudinal spherical aberration (LSA). The height at which these rays intercept the paraxial focal plane is called transverse spherical aberration (TSA).

Spherical aberration is dependent on the shape, orientation, conjugate ratio, and the refraction index of the lens. This means that in any optical set-up, slight misalignments or flaws in making of the lens can be detrimental in imaging applications. The elimination or reduction of spherical aberrations is usually done at the manufacturing level. In addition to improving polishing techniques for lenses, positive lenses (convex) and negative lenses (concave) can be combined to form lens combinations that compensate for spherical aberration. This type of compensation is most commonly found in objective lenses. The objective lens used in this thesis project is a Nikon 60x Plan Apo oil immersion objective lens, which means it already contains a series of positive and negative lenses to correct for spherical aberration. It is difficult and almost unrealistic to apply similar corrections to the rest of the lenses in the set-up. Instead, spherical

aberrations, or any type of aberration that is encountered in this project for that matter, can be corrected using software. Zernike polynomials are used to correct common types of aberrations. The Zernike polynomials will be introduced in Chapter 4.

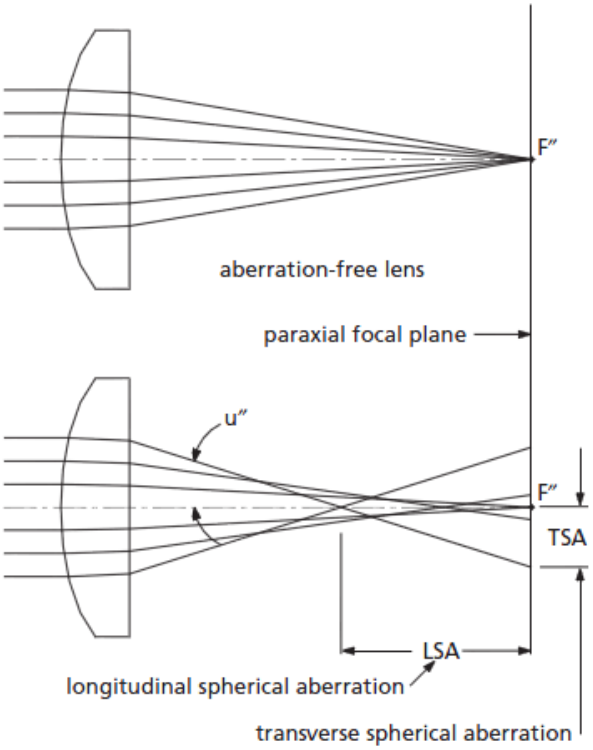

Figure 8. Ray tracing through an idealized aberration-free lens (top) and spherical aberration through an imperfect lens (Griot 2011)

2.3.2 Astigmatism

When an off-axis object is imaged by a lens, the asymmetry leads to astigmatism, which is when the imaging lens appears to have two different focal lengths, as illustrated in Figure 9. Tangential rays from the object come to a focus closer to the lens than do rays in the sagittal plane. Between the two conjugates, the image of a point-like object may look elliptical and blurry. This type of aberration is normally only dependent on the lens shape when there is an aperture in the system that is not in contact with the lens.

Astigmatism may occur when light is passing through the pinhole situated in between the beam expander in the optical set-up that will be discussed later, therefore it may become a concern, but it, too, can be corrected using Zernike polynomials.

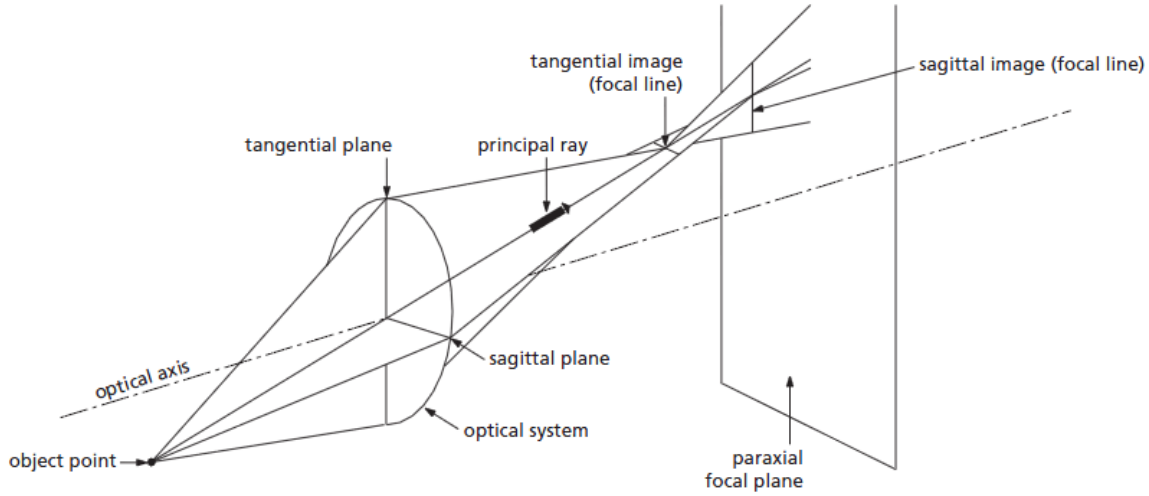

Figure 9. Ray diagram that illustrates how imaging off-axis objects can cause astigmatism (Griot 2011)

2.3.3 Coma

Different parts of the lens surface exhibit different radius of curvature and different degrees of magnification. Due to this property of a simple lens, each concentric zone of a lens forms a ring-shaped image called a comatic circle, as seen in Figure 10. This causes blurring in the image plane (surface) of object points that are off-axis (from the optical axis), which does not produce a sharp image, but has a characteristic comet-flare appearance. This type of aberration is known as coma and can be corrected for using Zernike polynomials.

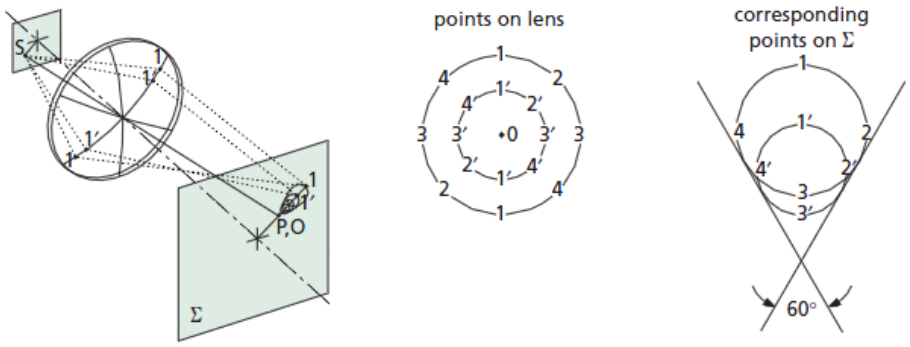

Figure 10. Comatic circle of lens with positive transverse coma (Griot 2011)

2.3.4 Distortion

Distortion is another commonly encountered aberration, where even if a perfect off-axis point image is formed, its location on the image plane is offset from the focal plane. Fortunately, this type of aberration is normally found in imaging applications, and for optical tweezers that have almost no spatial detail, distortion becomes a lesser concern. There are typically two main types of distortion: pincushion and barrel, as seen in Figure 11. Two lenses with opposite types of distortion can be combined to cancel the distortion effect and produce a distortion-free image.

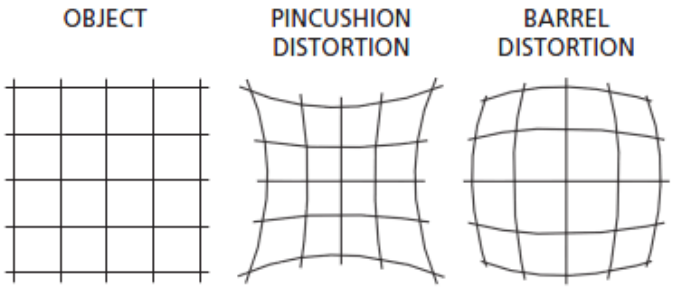

Figure 11. Types of distortion (Griot 2011)

2.4 Discussion

The key concepts of optical micromanipulation using SLMs were presented in this chapter. Light carries both wave and particle properties. The amplification process of

laser emission was introduced. Light emitted from a laser is always coherent; an emitted photon will always share the same wavelength and phase of the incident photon due to resonance. The fundamental principles of optical tweezers were then introduced. The dual nature of light works in conjunction to produce scattering and gradient forces on a dielectric particle, over which the forces together are able to impart 3D control. A simple aspheric lens can Fourier transform light by translating phase information to intensity information. The function of the LCoS spatial light modulator was then introduced, followed by a discussion on how phase holograms on the SLM can be translated into intensity space using a simple lens to create a desired 3D image. The chapter concludes with an introduction to the different types of aberrations that may occur during holographic micromanipulation. In the following chapters, it is shown that the aforementioned aberrations may be corrected for by superimposing two dimensional polynomial functions onto the programmed hologram to be displayed on the SLM.

Chapter 3 Holographic Optical Cell Rotation Preparation

3.1 Introduction

There are many methods in which SLMs are used, and hence optical set-ups may vary from one application to the next. However, there are some fundamental components that are always found in a basic holographic optical set-up in order for the basic Fourier principles to work. One such example will be the transformation lens that Fourier transforms the reflected light from the SLM to image space. These components and their functions will be introduced in the following sections. Another important factor for setting up an experiment for optical cell rotation is the properties of the cells being imaged. It is important that the cells are suspended and not adherent to the glass slide on which it is being imaged. For standardized experimentation, it is therefore essential to select the most suitable cell line that will either not adhere to the glass slide, or cell preparation procedure which will not affect the cells while preventing them from adhering to surfaces. Finally, it is important to consider how the optical tweezers should interact with the cell in order to maximize power efficiency and rotational stability. Two optical cell rotation methods were proposed in the end of this chapter. Experiments were conducted and results are presented in Chapter 5.

3.2 Optical Set-up

A 1064nm 4W DPSS laser source (Beijing Viasho Technology Co., Ltd.) was used as the primary laser source throughout the experiment. After the emitted laser beam was collimated with a collimator lens (f = 200mm), polarized and phase modulated, it was expanded by a 1:4 beam expander (f_1 = 50mm : f_2 = 200mm) so as to just overfill the microdisplay surface panel of the phase-only SLM (PLUTO, Holoeye photonics, AG,

1920 x 1080, 8μm × 8μm pixel size). A 75μm diameter pinhole (Newport, High-Energy Pinhole Aperture, 910PH-75) was placed at the focus between the two lenses to reduce scattered and incoherent light inherent in the laser. The suitable pinhole size was determined by measuring the beam width of the laser and to calculate the focus spot size of the 50mm lens. The laser beam width was measured using a beam profiler (Thorlabs, BP109-UV). The size of the focus spot as it exits the 50mm lens can be calculated using the following equation:

$$focus\ spot\ size = \frac{2f\lambda}{D}$$

where f is the focal length of the focusing lens, λ is the operating wavelength, and D is the diameter of the incident laser beam. For a Gaussian laser beam profile, the effective beam width is calculated by multiplying the maximum beam intensity by $1/e^2$. The $1/e^2$ width of the laser before it enters the lens is measured to be 2 mm using a beam profiler. The size of the focus spot is therefore calculated as follows:

$$spot\ size = \frac{2 \times (50) \times (1064 \times 10^{-6})}{(2)} = 0.0532mm = 53.2\mu m$$

A pinhole slightly larger than 53.2μm must be used; a 75μm pinhole is hence adequate for this optical set-up.

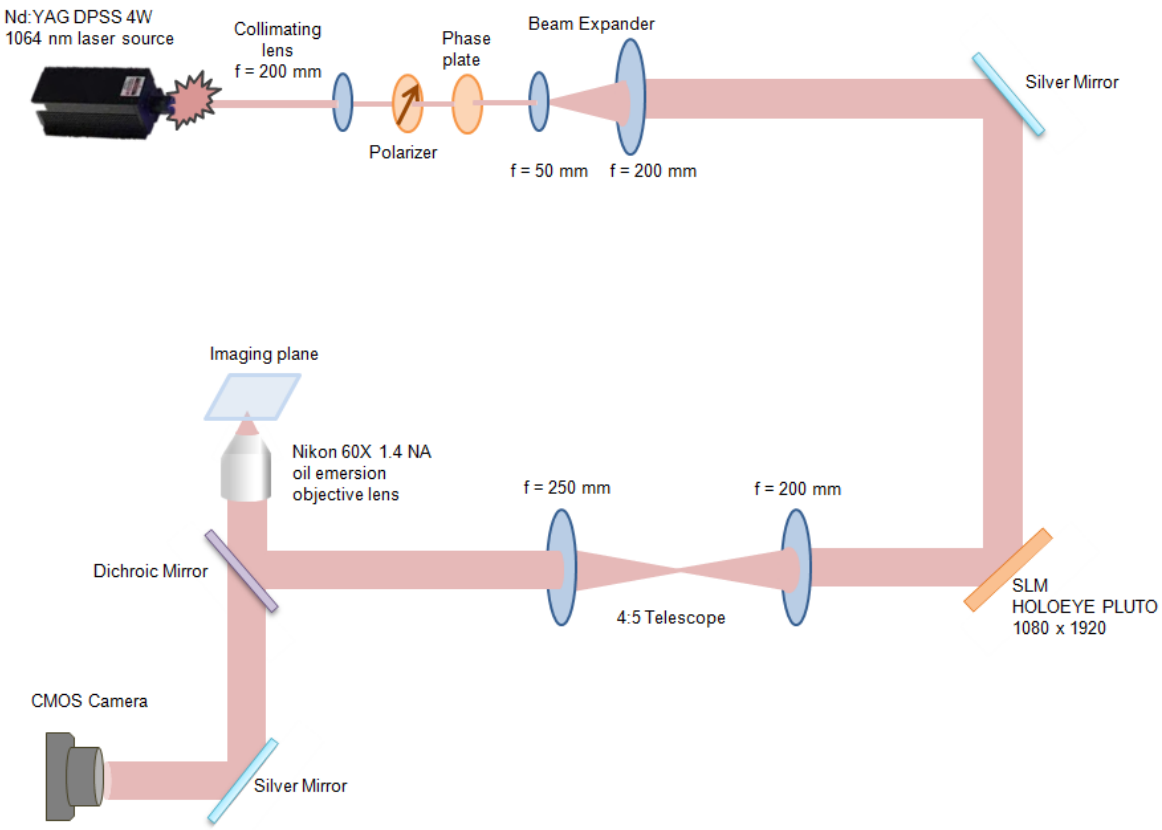

Figure 12. Optical set-up for holographic optical cell rotation experiments

Each pixel on the SLM contains a liquid crystal that can be independently addressed by the user digitally via a conventional DVI connection; in other words, the SLM microdisplay acts like an extended computer monitor. The input electronic voltage signals can alter the optical properties of the embedded liquid crystals in such a way that allow them to introduce phase shifts on the incident light from 0 up to 2π as it is being reflected away from the SLM. Interactive software created on LabVIEW generates input signals that are sent to the SLM in the form of grayscale phase masks, i.e. holograms. The pixel values on the holograms translate into phase shift values for each pixel on the SLM. The methods and algorithms applied to generate these holograms will be discussed in detail in Chapter 4. The reflected beam then passes through a 4:5 (f_1 = 200mm: f_2 =

250mm) telescope, where the beam is recollimated, and the size of the beam is readjusted to just slightly overfill the back aperture of the objective lens. The readjusted beam exits the telescopic lens system, and reflects off of a dichroic mirror to enter the objective lens (Nikon, Oil Immersion, Plan Apochromat, 60X, NA 1.4), at the focal plane of which the optical tweezers are produced. The image formed by the objective lens passes back down through the dichroic mirror and a short pass filter (FGS900) into a CMOS camera (Thorlabs, Inc., DCC1545M-GL), where the activity of the cell and the tweezers are recorded in real time. Figure 12 provides a schematic of the entire optical set-up. Images of the optical set-up and their components can be found in the Appendix.

3.3 Cell Preparation

Polystyrene beads (Duke Scientific Corporation, 5μm G0500) were used to test the initial set-up and performance of the optical tweezers before transitioning to testing on cells. The cells used throughout this thesis project are K562 human leukemia cells. K562 are naturally suspended in media and are spherical in shape, which make them an ideal candidate as a cell model. Owing to its inherent properties, no chemical treatment is necessary to rotate them in media, thus they can be maintained in a state as close to their physiological state as possible.

3.4 Investigation on the Optical Path of the Optical Tweezers

There are two proposed methods of exerting torque on the cell, and they differ only by the pathway in which the traps move along the cell. Figure 13 provides an illustration of both methods. In the first method (left), two traps start from either side on the equator of the cell, and move axially in a vertical path in opposite directions. Once the traps reach maximum depth (which is dependent on the diameter of the cell), they have

completed a single cycle, and the traps will instantly return to the starting position, where they will start a new cycle in this manner repeatedly.

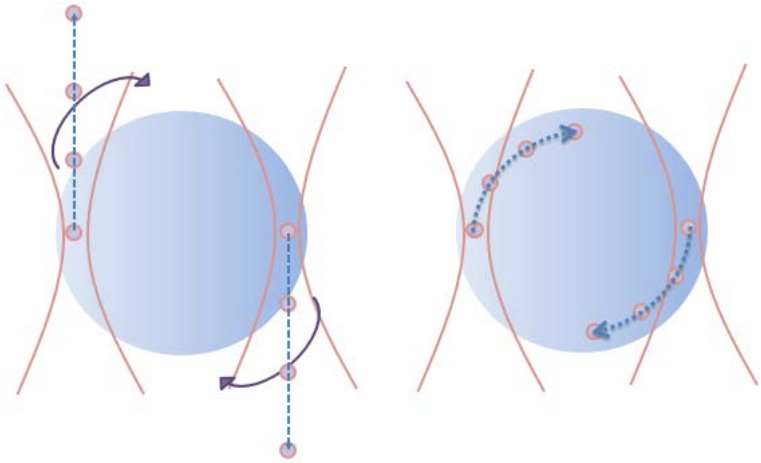

Figure 13. Optical pathways of SLM generated optical tweezers for optical cell rotation

The second method of rotation is similar to the first, except that instead of moving vertically, the traps move along the circumference of the cell. The traps must start and end at a position slightly off central axis to avoid singularity problems. Singularity is encountered when two traps are generated on the same lateral position. If the traps were not generated at an offset position from the center of the cell, when the traps start and end at the center position, the light that generates them will interfere and cause distortion and lead to problems with trapping stability. The lateral and axial offset of the starting position is calculated by setting an offset angle, as illustrated in Figure 14. The offset angle is determined by the number of frames generated in a single motion cycle. Tests were run to optimize the number of frames generated, and the results for the comparison between the two methods are summarized in Chapter 5.

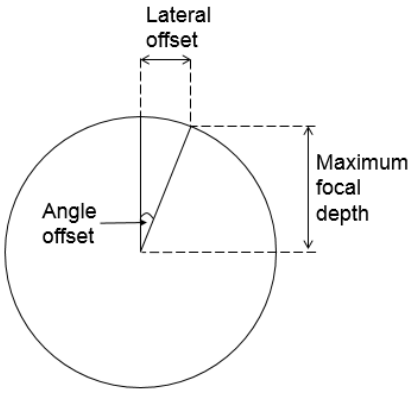

Figure 14. Relationship between angle offset with the lateral offset and the maximum focal depth

3.5 Discussion

The optical set-up for the entire project was provided in detail, followed by a basic introduction to the two proposed methods of cell rotation. Essentially, the first method relies on the inertial forces generated by the vertical motion of the traps to induce continuous rotation. The second method requires that the individual tweezers physically trap a part of the cell, likely an organelle, and keep it constantly trapped during the entire rotation. The motion of the trapped entity of the cell will cause the cell to reorient itself with respect to their positions. The results are presented in Chapter 5.

Chapter 4 Hologram Generation using LabVIEW

4.1 Introduction

Similar to photography, holography is a method that records light from objects, and then translates and reproduces them in the image space. However, holography is capable of much more than photography. Photography records optical distributions as optical density is given by intensity only, which means phase information is lost in photography. Without phase information, a photograph will have no depth information, making image projections appear only in two-dimensional space. Holography, on the other hand, records and retains phase information, which can be encoded in a complex distribution. This way, both intensity and phase information can be captured in a complex form, and can be reconstructed using theories in Fourier optics. Images that are reconstructed from light that was adjusted or structured via wavefront modulation devices can thus be projected in 3D space.

Holography captures reflected light from a three-dimensionally complex structure, such as a statue, by shining an object with a coherent reference beam, and recording the resultant scattered and reflected light. Here, phase information is not lost, therefore the light recorded can be used to computationally reconstruct the 3D surface of the figurine by emulating the distribution of the images using a wavefront correction device. For dynamic optical tweezers, the recording of an object is not necessary. The desired position and shape of each of the traps are already known, so we can produce these images using relatively simple algorithms to create their corresponding holograms. There are two main approaches to generating holograms. They can be generated either iteratively or analytically. The type of algorithm to use depends on the complexity of the

image that is being generated. Since the 3D images of interest in this project are simple Gaussian traps, the holograms for these traps can be generated analytically using the lenses and gratings algorithm (Leach et al. 2006), which is described in following sections. In contrast, the Gerchberg-Saxton algorithm (Zalevsky, Mendlovic, and Dorsch 1996) is an iterative method that is a fairly common method for generating holograms for optical trapping applications. The following sections will provide an overview of the basic algorithms used throughout the entire thesis.

4.2 Blazed Gratings

Images from the SLM are formed by the laws of diffraction. The SLM can be used to control the diffraction order at which the images are generated. Typically, images are formed at the first order due to higher efficiency, but other orders can also be used depending on the operating wavelength as well as the blaze angle of the diffraction grating used. The zero order is the beam of light that is unaffected by the SLM. Generally it is desirable to avoid imaging with the zero order in sight or around the generated optical traps, not only because it serves no function on the image plane, it also produces a gradient force that may compete with the attraction force generated by the optical tweezers, resulting in reduced trapping efficacy and efficiency. In addition, it may possibly cause asymmetric trapping strength between the two generated traps and lead to unstable rotation. In order to maximize the amount of power being transferred from the zero order to the optical tweezers, a blazed grating is traditionally used. A blazed grating is an optical element that contains a series of small reflective triangular teeth-like gratings that can reflect incoming light (i.e. zero order light) at an angle, and the order of diffraction at which the image is produced is determined by the steepness and periodicity

of the gratings. Since the grating is essentially altering the phase of light using a series of slopes, the grating effect of diverting light from zero to first order can be emulated using holograms displayed on a SLM; this is the most common method of directing zero order intensity to first order intensity (Breidne et al. 1979; Wang et al. 2000; van der Horst, Downing, and Forde 2009).

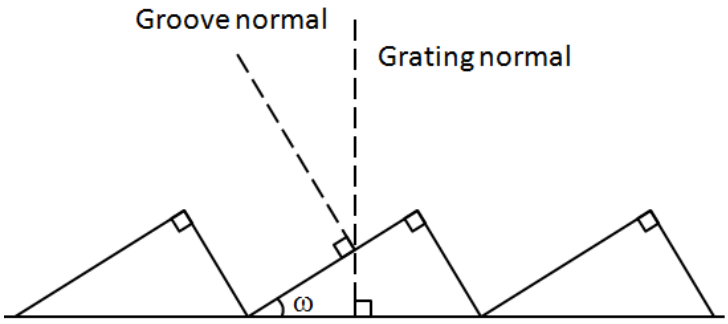

Figure 15. Outline of blazed grating with blazed angle

4.2.1 Scaling

The blazed grating is a type of diffraction grating that is used to direct the light of a limited region of the spectrum into any order other than the zero order. Blazed gratings are designed to produce maximum efficiency at designated operating wavelengths. The gratings are made up of grooves that are raised at a blazed angle ω, to form right angled triangles as shown in Figure 15. The grooves' profiles are calculated for the Littrow condition where the incident and diffracted rays are in auto collimation (i.e. $\alpha = \beta$). In other words, the output rays propagate along the same axis as the input rays at the blazed wavelength λ_B. The equation for the Littrow condition is as follows:

$$2 \sin \omega = \frac{m\lambda_B}{d}$$

The blazed grating can used to control the x-y lateral position of optical traps, as it can divert light at any x-y position at high efficiency. The effect of blazed gratings can be

simulated on the SLM using grating phase diagrams, where the grooves become grayscale ramps with a specific grating period. The grayscale values range from 0 to 255, and scaled from 0 to 2π on the SLM. Figure 16 is an example of a phase diagram for a blazed grating.

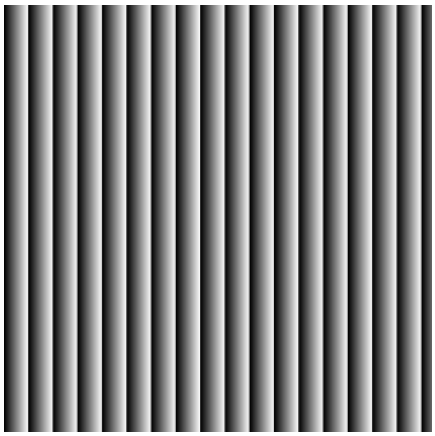

Figure 16. Sample hologram of a diffraction grating

Grating periods can be calculated given the desired distance of the first order from the zero order and the magnification factor through the optical set-up. To generate a trap at distance x_{trap} away from the zero order on the image plane (i.e. at the objective lens), the equivalent distance x_{SLM} at the object plane (i.e. at the SLM) must be known:

$$x_{SLM} = \frac{x_{trap}}{M}$$

where M is the magnification of the optical path:

$$M = \frac{f_{obj}}{f_1}$$

The focal length of the first telescopic imaging lens on the optical path f_1 is 200mm (refer to Figure 2.1). The focal length of the objective lens f_{obj} is a function of the tube length of the objective lens. Tube length may vary from one lens manufacture to another.

Typically, a Nikon objective lens has a standard tube length of 200mm. The focal length of the objective lens can thus be calculated using the following relationship:

$$f_{obj} = \frac{tube\ length}{magnification\ power} = \frac{200mm}{60X} = 3.33mm$$

$$\therefore M = \frac{3.33mm}{200mm} = 0.0167$$

and

$$x_{SLM} = \frac{x_{trap}}{0.0167}$$

To find the angle at which the SLM is required to diffract the beam in order to create a displacement of x_{SLM} (just computed), use simple trigonometric relationships from Figure 17:

$$\tan\theta = \frac{x_{SLM}}{f_1}$$

The period of the grating *d* is finally calculated using the diffraction grating equation:

$$d\sin\theta = m\lambda$$

where θ is the angle of diffraction, *m* is the order of diffraction, in which case *m* = 1, and λ is the operating wavelength (1064nm). Using the aforementioned geometric relationships, the correct displacement can be calculated at any coordinate within the field of view of the x-y plane.

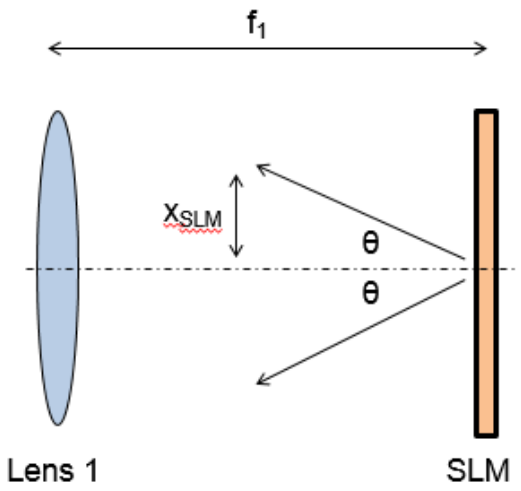

Figure 17. Trigonometric relationships between lateral displacement, focal distance and angle of diffraction

4.2.2 Blazed Grating Ramp Methods

Three different ramp grating phase designs were compared to investigate their efficiency in diverting zero order power to the first order traps. Figure 18 shows the different types of grating designs tested in this thesis. Periodicity was calculated using the method discussed in the previous section. The first method is the traditional simple blazed grating described previously. In the second method, right triangles with a blazed angle were placed on top of a ramp grating. The third method was to have step-wise ramps replace the gratings in the first method. The reason for these alternate designs was to ensure that maximum power is conserved and transferred to the traps. The results for this comparison are presented in Chapter 5.

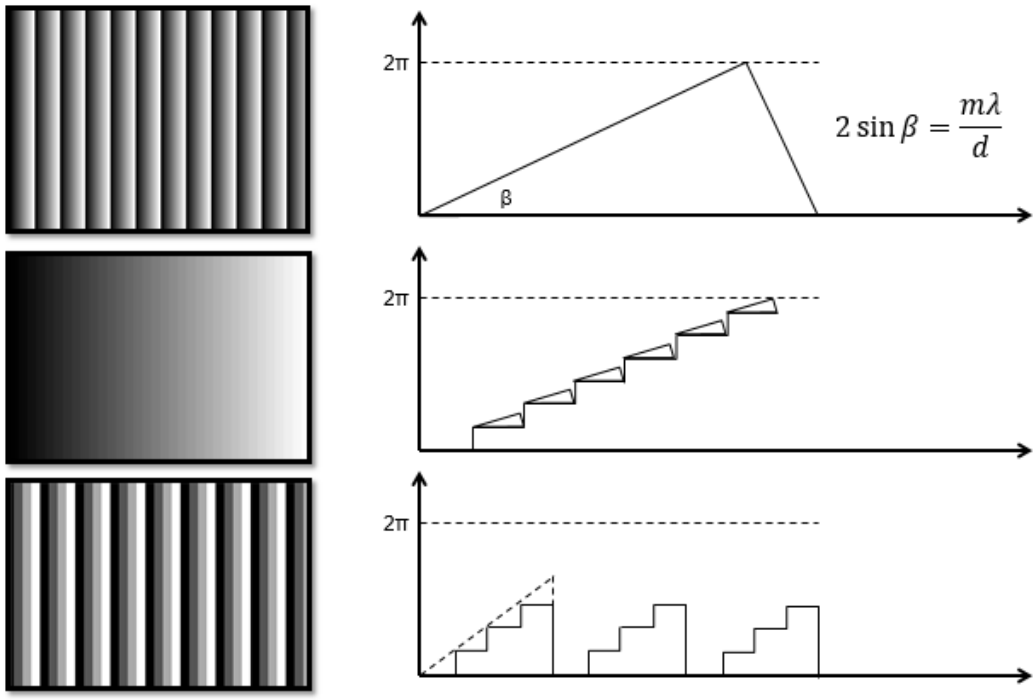

Figure 18. Diffraction grating designs

4.3 Fresnel Gratings

To have true 3D control over a cell, z displacement control must be added to the blazed grating holograms that only controls lateral displacement of the traps. To move the optical traps axially, Fresnel gratings can be used. Fresnel gratings are essentially concentric edged gratings as seen in Figure 19. Fresnel gratings on the SLM emulate the effect of Fresnel zone plates, and like the blazed grating, can be generated analytically (Miyamoto 1961; Carcolé, Campos, and Bosch 1994; Rosen et al. 2009). By adjusting the focal length of the Fresnel grating, the image will shift relative to the focal distance of the imaging lens (i.e. the objective lens). The two-dimensional mathematical function for the Fresnel grating phase distribution is:

$$\varphi_{Fresnel,ij} = \frac{k\left(\left(x_{ij} - x_0\right)^2 + \left(y_{ij} - y_0\right)^2\right)}{\lambda z} mod(2\pi)$$

where $\varphi_{Fresnel,ij}$ is the phase value for pixel on row i and column j; k is the wave number; x_{ij} and y_{ij} are the x and y positions of the pixel being addressed in a distance scale; x_0 and y_0 are the coordinates of desired location of the trap scaled to the image distance space of the SLM; λ is the operating wavelength (i.e. 1064nm); z is the focal length of the desired Fresnel grating. Modulo 2π operation is necessary to create the ridges with the periodicity of a Fresnel grating. The x_{ij} and y_{ij} distance is the distance of the pixel being addressed from the top left hand corner of the SLM panel, and is proportional to the pitch size of each pixel on the SLM. The pixel pitch size for the SLM is 8μm (i.e. each pixel can be thought of as being is 8μm by 8μm), therefore to compute x_{ij} and y_{ij}, which reflects the true distance of the pixel on the SLM, multiply the indexes of the column and row with the pitch size.

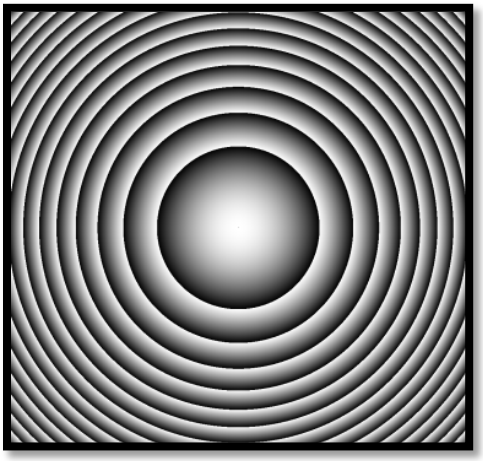

Figure 19. Fresnel zone plate

Ideally, the region exposed to the highest laser intensity is the center of the SLM, so the center of the Fresnel zone plate grating should also be displayed at the center of the SLM instead of the top left hand corner as indicated by the Fresnel equation. To center the Fresnel grating, simply add the half length or half width to the coordinates x_0 and y_0,

so that index (0,0) addresses the pixel at the center of the SLM. Fresnel gratings are also capable of controlling the lateral positions of images. The input x, y, and z distance offset (in μm) from the center is read in by the program and converted to the distance at the SLM by taking into account the magnification of the system. The desired distance is divided by the magnification factor *M* to give the pre-transformed distance.

To scale the depth displacement at the objective lens correctly to the focal length of the Fresnel grating, the simple lens equation can be used:

$$\frac{1}{f} = \frac{1}{i} + \frac{1}{o}$$

where *f* is the focal length of the transformation lens; *i* is the distance of the image from the lens; and *o* is the distance of the object from the lens. Figure 20 shows the interface of a sub-VI written in LabVIEW. It calculates the required focal distance of the generated Fresnel grating in order to produce the specified axial displacement, which is the input data. Knowing the focal length of each of the lenses used in the set-up and knowing the distances between each optical element, the "object" distance o_M of the trap can be easily calculated. The distance of that "object" will then be subtracted from the distance between its imaging lens and the preceding lens to determine the image distance from the preceding lens.

An example of the calculation of the Fresnel focal length is shown below. If a trap displacement of i_M = 10μm = 0.01mm is desired (i.e. the trap is 10μm above the focal plane of the objective lens), then:

$$o_M = \frac{1}{\frac{1}{f_M} - \frac{1}{i_M}} = \frac{1}{\frac{1}{3.33mm} - \frac{1}{0.01mm}} = 1.11422m$$

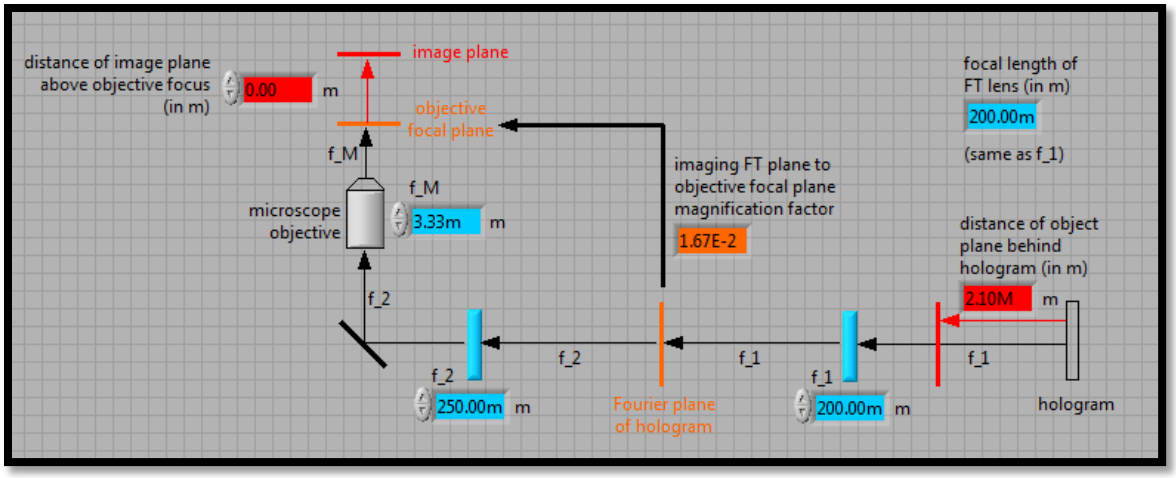

Figure 20. LabVIEW interface of lens relationships in optical set-up

The image of lens 2 will then equal the difference between f_2 and the calculated object distance from the objective lens o_M, which is$0.25 - 1.11422 = -0.864817m$. Since the image distance i_2 is a negative number, the image will be behind lens 2.

$$o_2 = \frac{1}{\frac{1}{f_2} - \frac{1}{i_2}} = \frac{1}{\frac{1}{0.25m} - \frac{1}{(-0.86m)}} = 0.193907m$$

Similarly, the distance of the image formed by lens 1 is$(f_2 + f_1) - o_2 = (0.25 + 0.2) - 0.19 = 0.256093m$. Using the lens equation, the calculated estimated object distance o_1 is 0.913099 m. The focal length of the Fresnel lens to be generated will then be f_1 – 0.26 m = -0.713099 m, which is again “behind” the Fresnel lens (i.e. the SLM). It is possible to produce the resultant image at any distance from either side of the lens. When the calculated focal length is positive, this means that the image is generated in front of the SLM, or the Fresnel lens is convergent; if the estimated focal length is negative, the generated image is “behind” the SLM, or the Fresnel lens is divergent. The simple algorithm will create accurate trap displacements on the image plane of the objective lens. The Fresnel lens hologram is superimposed on the blazed grating hologram to create

a single hologram that controls the trap in three dimensions. This method of combining these two analytical grating holograms is conventionally called the “gratings and lenses” algorithm. The method of combining these holograms will be discussed in later sections.

4.4 Gerchberg-Saxton Algorithm

Another two-dimensional method of generating holograms on the x-y plane is to use an iterative algorithm called the Gerchberg-Saxton algorithm (GSA) (Zalevsky, Mendlovic, and Dorsch 1996; Engström et al. 2009). This method is commonly used to generate holograms for complex images or text, but it can also be used to generate simple patterns such as optical tweezers. This iterative method uses Fourier optics theory to estimate the phase information of the desired intensity distribution of an image. Phase distribution of the image is necessary because phase information is what forms shapes and edges of an image; phase controls the spatial organization of an image. Figure 21 provides a schematic for the computational process of determining the phase distribution of a desired image. First, start with a known light source intensity profile, which is commonly a coherent Gaussian beam just like a laser light source. Assume that the phase information of the initial intensity is the profile of a Gaussian beam with zero phase information. This amplitude information is Fourier transformed as if passing through a lens to form an image that would eventually resemble our target intensity. The result is a solution with a real part and a complex part. The real values represent the intensity of the output light which will converge closer and closer to the desired image intensity upon each iteration; the imaginary values resemble our phase. On the other hand, the target intensity is known as two traps at two different positions. This target image, which begins with only real amplitude values, is combined with the extracted imaginary part of the

Fourier transform of the pervious source intensity to produce a target image with both intensity and phase information. This image is inverse-Fourier transformed, producing both intensity and phase information; the phase array is essentially the corresponding estimated hologram, and each pixel value can range from 0 to 2π. This phase information is integrated with the target intensity information. As this phase information is extracted and is combined with the source intensity to form another complex array, this array is in turn Fourier transformed, thereby producing an intensity distribution that may begin to resemble the target image due to the added phase values. This intensity information is compared with the target image to produce an error value. If the error is higher than the threshold error value, then the resultant phase array will be passed down to be combined with the target intensity and inverse-Fourier transformed again, to produce a more accurate hologram. When the iterated intensity distribution resembles the target intensity within a certain error, then the iteration is terminated, and the resulting hologram is displayed on the SLM to create the image.

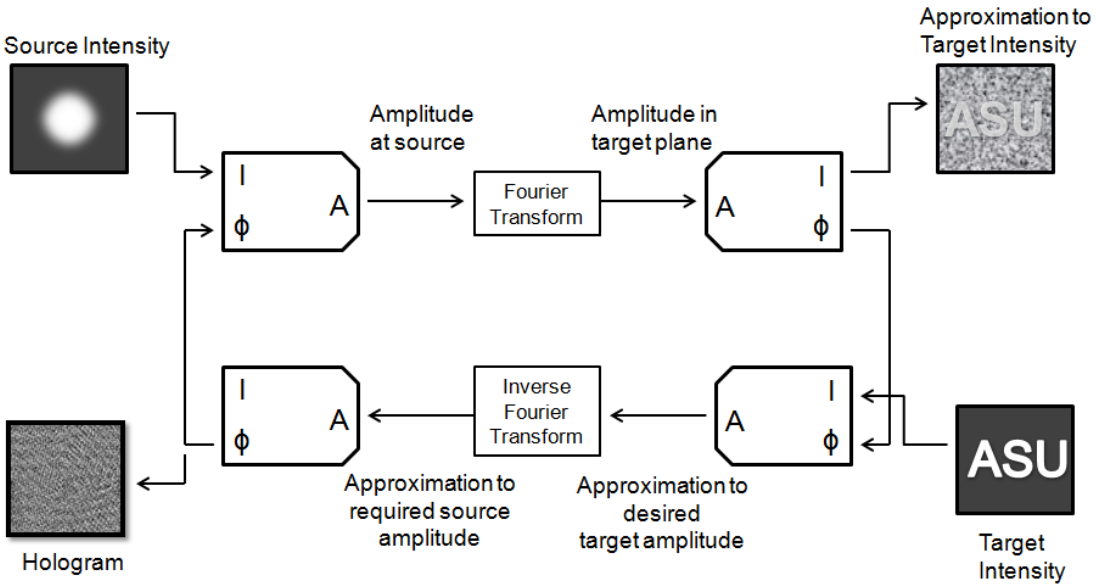

Figure 21. Schematic for the Gerchberg-Saxton Algorithm

4.5 Random Binary Mask Algorithm

In order to create dynamic optical traps at video rate, the computation time of holograms becomes an important factor when selecting the algorithm to use. The random binary mask algorithm is widely applied for interactive optical tweezers generation over the past decade due to its advantages with speed and computational cost. This method is an adaption of the random-mask encoding technique (Montes-Usategui et al. 2006; Davis and Cottrell 1994).

This method essentially divides the SLM into as many subdomains, I_k, as optical tweezers are needed. Each subdomain will occupy an equal amount of pixels on the SLM, and have pixels that are randomly dispersed over the SLM display. To generate only two traps, a simple binary random mask array with the identical dimensions as that of the desired hologram dimensions can be generated. If more than two traps are desired, then a multiplexed mask will be needed. For this thesis, two traps must be created, therefore a binary mask will suffice. Holograms for individual optical traps are produced analytically via the gratings and lenses algorithm described in previous sections. For the binary case, the hologram of trap 1 will be displayed on subdomain I_1 while the hologram for trap 2 will occupy subdomain I_2 on the SLM, as shown in Figure 22. Since each subdomain occupies the same amount of pixels that are randomly dispersed over the SLM, each hologram is assumed to be exposed to approximately the same amount of light intensity, so as to ensure equal trapping power between the traps.

A binary mask with 1080 x 1080 pixels was generated, and each pixel contains a value of either zero or one. Instead of altering individual pixels randomly, random blocks of 10 x 10 pixels were addressed. Imagine that each individual colored block in Figure 22

is actually comprised of a 10 x 10 array, or 100 pixels, and each pixel within that block is allocated the same binary value. Several random distributions of the blocks were generated, and tested on the SLM to ensure even intensity distribution between the two holograms. The best performing distribution was saved as a customized binary mask, and reused for repeatability as well as lowering computational cost, such that a 1080 x 1080 array of random binary numbers does not have to be generated each time a new hologram is computed.

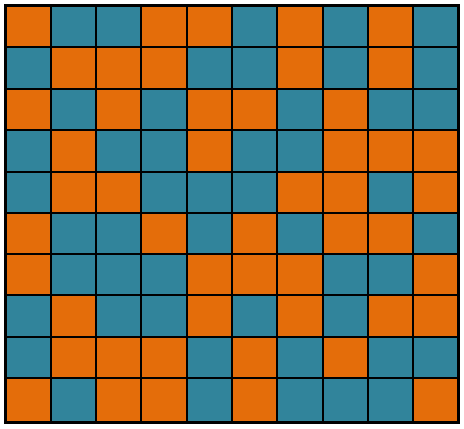

Figure 22. Random distribution of contents in two different holograms represented by different colors

Approximately 50% of the pixels on the SLM were allocated for the hologram of trap 1, and the other half was allocated for the hologram of trap 2. This is done by taking the dot product (cell to cell multiplication) of the binary mask array and the hologram of the first trap. A negative of the binary mask is then taken, and multiplied by the hologram of the second trap. The two separate holograms are added together to create a single hologram for two separate traps. An example of a hologram generated by the random binary mask algorithm is shown in Figure 23.

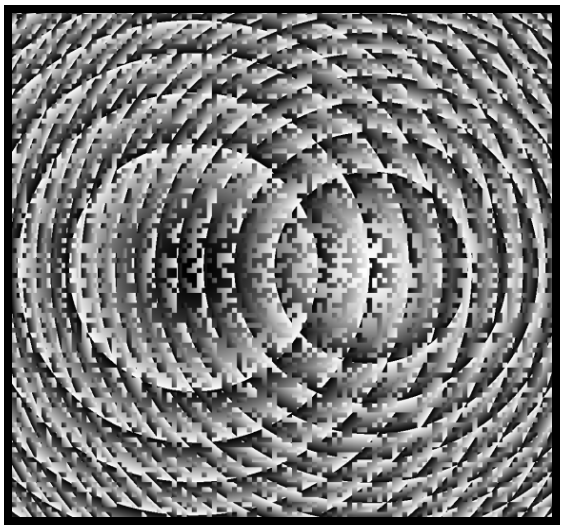

Figure 23. Hologram of two Fresnel gratings combined by the Random Binary Mask Algorithm

4.6 Methods of Combining Holograms

Holograms can be overlaid on top of one another using a modulo 2π operation. This does not cause phase information to be lost, because phase only cycles through 0 to 2π, where 3π and π is essentially at the same phase of a single wave cycle. The modulo 2π operation will combine the effect of the each added hologram to create a single hologram to be displayed on the SLM. The gratings and lenses algorithm uses this technique to combine the blazed grating hologram with the Fresnel grating hologram to control position of the image three-dimensionally. The combination of a single blazed grating with a Fresnel grating makes a hologram for a single trap. A second trap can be added onto the hologram using the random binary mask function. Although the two holograms can also be overlaid with each other using the modulo 2π function, it is found that it is less efficient and is prone to forming ghost traps (Hesseling et al. 2011; Montes-Usategui et al. 2006).

Two methods of combining holograms were explored in this study. They differ merely in the sequence in which the gratings were superimposed, but it resulted in very different image properties that will be discussed here. The first method applies the random binary mask algorithm onto two Fresnel gratings. Instead of using the blazed grating to control the lateral position of the trap as described previously, the position of the trap corresponding to the Fresnel hologram is controlled by adjusting the position of the annular center of the Fresnel zone plate relative to the center of the hologram. A single diffraction grating is overlaid on this random binary hologram only to wean the two traps away from the zero order by using the modulo 2π operation.

Oddly, the lateral position of the traps generated by this method deviates further and further away from the center of that in theory as the axial distance of the trap from the focal plane increases. The straying of the foci was non-linear, making it difficult to characterize and compensate for. This shift is likely caused by aberrations in the lenses, which is quite unavoidable since optical set-ups such as this is mostly assemble by hand, and is prone to human error. Figure 24 shows a rough description of the non-linear path in which the lateral shift follows as the depth increases.

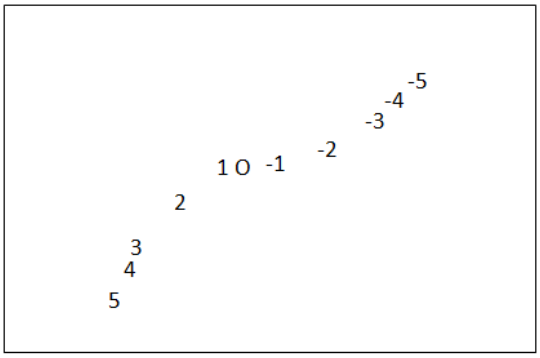

Figure 24. Straying path of traps along the axial axis: The higher the numbers, the further away it is from the 0 focal plane of the objective lens

Although the reasons behind the lateral shifting of the traps are not well understood, experimentation with the sequence of overlaying hologram eventually led to a new method in which the hologram is less sensitive to minute optical misalignments. This requires only a slight modification to the first method. The improved method first generates two centered Fresnel gratings with their respective axial displacements. Unlike the previous method, the lateral position is controlled by two separate blazed gratings with their respective periods depending on their respective lateral positions. The resultant two holograms, each with a different Fresnel grating and blazed grating superimposed on one another, are then combined into a single hologram using the random binary mask algorithm. This new method eliminates the unwanted lateral shifting that was observed in the previous method.

4.7 Generating Video Rate Hologram Sequences

So far, only the methods for generating a single hologram have been discussed. Ultimately, these individual holograms are compiled together to create a video sequence to be played on the SLM panel. There are two methods of displaying dynamic optical tweezers holograms on the SLM: the first option is to display the holograms on the SLM as they are generated on the fly; the second option is to generate and save each computed hologram as binary files in a folder, then create an AVI file using LabVIEW. Before selecting the best method for hologram display, some video parameters must be considered, such as frame rate, and number of frames per complete cycle (the displaying of the first frame to the final frame of the sequence is considered to be one cycle). Displaying the holograms on the fly is more convenient than generating binary files and later composing an AVI file. Unfortunately, the computational speed of the real-time

generation method is limited by the processor of the computer being used. Each pixel value (from 0 to 2π) on a hologram was represented by a single precision binary floating point number (SGL). This means that each pixel value consumes 4 bits of memory. Each hologram generated was a 1080 x 1080 pixel image. The computer used (Dell, 32-bit Windows 7 Professional, Intel Duo CPU Processor 3.0 GHz, 4 GB RAM) together with the LabVIEW software was, at maximum speed, only able to display holograms on the fly at a rate of 1 frame per second (fps). To generate video sequences with faster frame rates, the most straight forward way is to simply create a video file. LabVIEW contains a built-in utility that retrieves images frame by frame to generate AVI files at a user-defined frame rate. Each of these generated videos containing frames of holograms can be displayed on the extended monitor of the computer (i.e. the SLM display) in a loop. The maximum refresh rate for the SLM is 60Hz, so one must be cautious not to generate the video files at more than 60 fps. A disadvantage of this method is that it requires storage space for all the generated binary files and video files for a given set of parameters. The only way to change the parameters is to regenerate hologram frames and video files for each new set of parameters. A library of videos was generated for convenience. This video library contained hologram AVIs for tweezers that are 3μm to 20μm apart, each at frame rates ranging from 3 fps to 30 fps. A set of videos were generated at 75 frames, 100 frames, 125 frames and 150 frames per cycle.

4.8 Correction for Aberrations

Aberrations can be corrected using Zernike polynomials, which is a sequence of mathematical functions named after Frits Zernike, a Nobel Prize laureate and optical physicist, and inventor of phase contrast microscopy. Zernike polynomials were

originally developed to describe the diffracted wavefront in phase contrast microscopy, but have since made a great impact in the rest of the field of photonics and optics. Figure 25 shows the two dimensional beam profiles for each Zernike function. Table 3.1 lists the mathematical representation of the Zernike polynomials and the types of aberration each polynomial resembles.

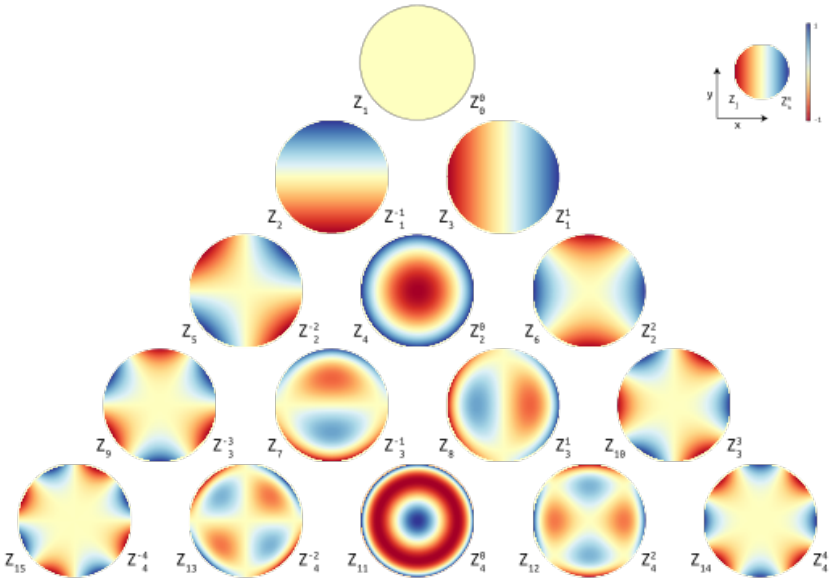

Figure 25. Two-dimensional representation of Zernike Polynomials

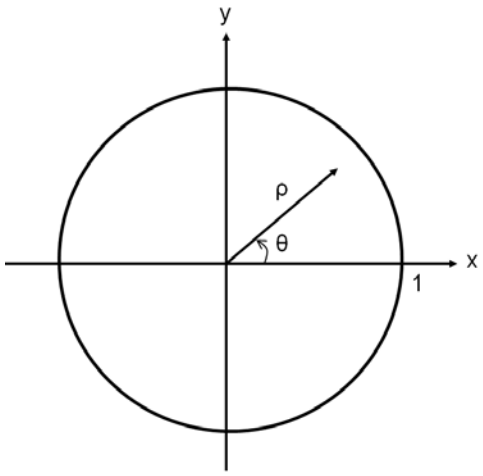

Figure 26. Unit Circle where ρ is the normalized coordinate and θ is the azimuthal degree

Table 1. Zernike Polynomials

Noll index (j)	Radial degree (n)	Azimuthal degree (m)	Z_j	Classical name
1	0	0	1	Piston
2	1	1	$2\rho\cos\theta$	Tip (x tilt)
3	1	-1	$2\rho\sin\theta$	Tilt (y-tilt)
4	2	0	$\sqrt{3}(2\rho^2-1)$	Defocus (longitudinal position)
5	2	2	$\sqrt{6}\rho^2\sin 2\theta$	Astigmatism
6	2	2	$\sqrt{6}\rho^2\cos 2\theta$	Astigmatism
7	3	-1	$\sqrt{8}(3\rho^3-2\rho)\sin\theta$	Coma
8	3	1	$\sqrt{8}(3\rho^3-2\rho)\cos\theta$	Coma
9	3	-3	$\sqrt{8}\rho^3\sin 3\theta$	Trefoil
10	3	3	$\sqrt{8}\rho^3\cos 3\theta$	Trefoil
11	4	0	$\sqrt{5}(6\rho^4-6\rho^2+1)$	Third order Spherical Aberration
12	4	2	$\sqrt{10}(4\rho^4-3\rho^2)\cos 2\theta$	Fourth order Astigmatism
13	4	-2	$\sqrt{10}(4\rho^4-3\rho^2)\sin 2\theta$	Fourth order Astigmatism
14	4	4	$\sqrt{10}\rho^4\cos 4\theta$	Quadroil
15	4	-4	$\sqrt{10}\square^4\sin 4\square$	Quadroil

In the Zernike polynomial equations shown in Table 1, ρ is the normalized coordinate that is calculated by dividing the real radial coordinate by the maximum radius; θ is the azimuthal frequency, as depicted in Figure 26.

Figure 25 shows the first 15 Zernike polynomials that are ordered vertically by radial degree, and horizontally by azimuthal degree. The zero order Zernike polynomials ($Z00$) on the top row is called Piston and is usually ignored. The surface is constant over the entire circle, so no error or variance exists. The first order Zernike polynomials (Z_1^{-1} and Z_1^1) on the second row represent the tilt in the wavefront. The combination of these terms results in a general equation for a plane. By changing the coefficients, a plane at any orientation can be created. This rotation of the pattern is true for the sine/cosine pairs of Zernike polynomials. The second order Zernike polynomials (Z_2^{-2}, Z_2^0, and Z_2^2) on the third row are the wavefronts that would results from Jackson crossed cyclinder J0 and J45 and an aspheric lens. Thus combining these terms will give any arbitrary spherocylindrical refractive error. The third order Zernike polynomials (Z_3^{-3}, Z_3^{-1} , Z_3^1, and Z_3^3) on the fourth row represent asymmetric aberrations that usually cannot be corrected using conventional lenses. The center two terms are for coma, while the outer two terms are for trefoil. The fourth order Zernike polynomials (Z_4^{-4}, Z_4^{-2}, Z_4^0 , Z_4^2, and Z_4^4) on the fifth row represent more complex shapes of the wavefront. The most commonly used set of polynomials would be Z_4^0 for spherical aberrations.

Similar to the blazed gratings and Fresnel grating functions, phase holograms can be generated analytically using these Zernike polynomials. They are combined with the uncorrected holograms using the modulo 2π operation to create the final hologram displayed on the SLM. It is highly improbable that a simple optical set-up such as that

presented in the thesis will require fourth order corrections, with the exception of spherical aberration corrections, therefore Z_4^2 and Z_4^4 were not integrated into the LabVIEW program. The Zernike LabVIEW utility was embedded into the main program as an add-on function that can easily be implemented or omitted as desired by the user. Since a cell may not be perfectly spherical, and contains many organelles of different optical properties that may distort the light passing through the cell, any minor aberrations will be magnified. Zernike corrections will therefore minimize the degree of beam profile distortion in the cell, and significantly improve the power efficiency and quality of rotation.

4.9 Discussion

This chapter introduced some basic algorithms to generate holograms, the lenses and gratings algorithm 3D position control; the Gerchberg-Saxton algorithm for more complex image structures; and the random binary mask algorithm for simultaneously displaying multiple holograms. In addition to the sequence in which the holograms are overlaid on each other, special care should be taken when determining the distance of the first order from the zero order. The further away the first order is from the zero order, the smaller the period of the grating. In that sense, the minimum period of the gratings generated is dependent on the pixel size and the number of pixels on the SLM display. This is an important factor to consider, because this loss of resolution on the period of the blazed grating may lead to aliasing, which causes ineffective movement of the generated trapping sequence. A way around this problem is to generate the pair of traps, each with large periods (much closer to the zero order), and then apply another blazed grating on top of the overall hologram to shift them further away from the zero order. The total

lateral shift will be additive, and will allow higher resolution lateral movements of the traps. Lastly, methods of correcting different aberrations were introduced. The most common type of aberration is spherical aberration caused by misalignments through the optical tract. These can easily be corrected using fourth order Zernike polynomials. The effects of Zernike wavefront correction is demonstrated in Chapter 5.

Chapter 5 Characterization of Optical Cell Rotation

5.1 Introduction

Once cells are rotating using the dynamic holographic optical tweezers generated by the methods described in Chapters 2 and 3, the rotation must be characterized and optimized for the single live cell CT system. Ideally, the rotation of the cell should be kept very stable so as to increase the accuracy of the reconstruction. Jittering can cause undesirable artifacts in the image, such as blur and noise. The more projections the cell CT system takes, the more data the reconstruction algorithm is provided with to generate the 3D image, and consequently the less uncertainty there is in the final reconstruction. To increase the yield of projections and simultaneously identify the angle at which the projection was taken, the rotation of the cell needs to be kept at as slowly as approximately one rotation per minute. This section will discuss all the adjustable parameters involved in the generation of the optical tweezers. Tests were run to study these parameters so rotation may be optimized, at which the cell can rotate slowly, continuously, and smoothly.

5.2 Laser Characterization

Before any experiments are done, the laser must first be characterized. The laser power output is controlled by a dial that is indexed from 1 to 10. The output of the laser needs to be characterized to determine at what power level the laser is operating, because it was immediately apparent that the output of the laser power and the dial index does not have a linear relationship. The measurements were done using a laser power meter (Coherent Inc, Air-Cooled Thermopile Sensors PM10 (RoHS)). Figure 27 and Figure 28

shows the relationship between the power output levels in watts and the equivalent dial index. These plots were used as a reference for setting power of the traps.

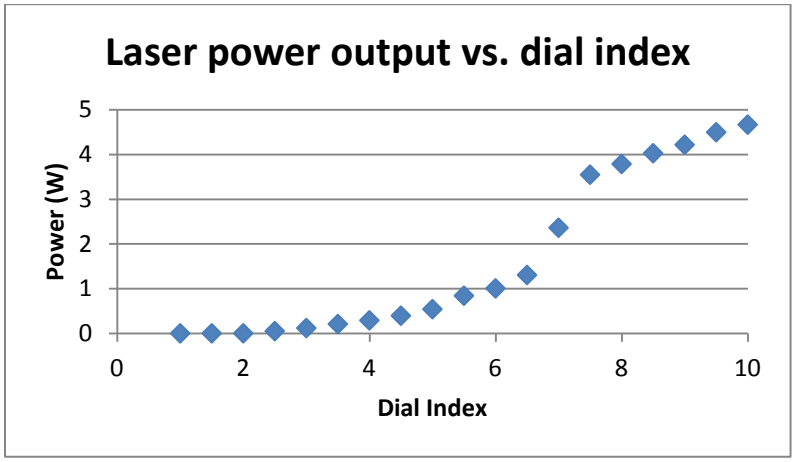

Figure 27. Characterization curve of Viasho Laser

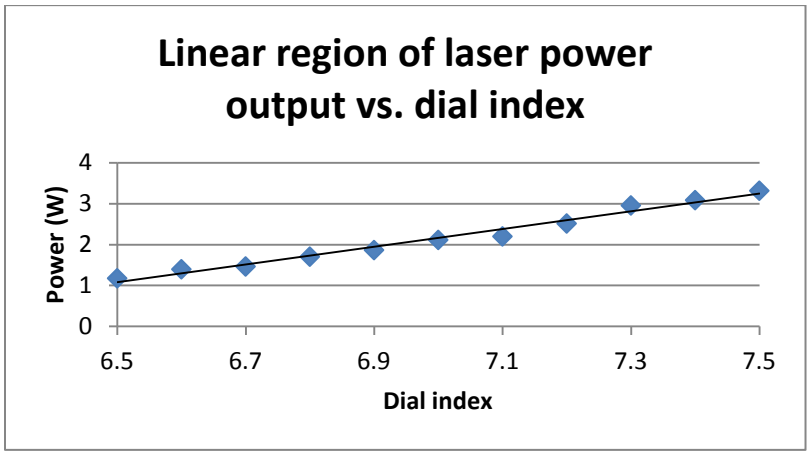

Figure 28. Linear region of Viasho Laser between 1W to 3 W

5.3 Parameters

There are many factors that can affect the stability and speed of cell rotation. Fortunately, by using dynamic holographic optical tweezers to rotate cells, most factors are controllable to a certain degree. Some uncontrollable parameters include the distribution of organelles or density within the cell, and these factors may cause unpredictable asymmetry in the cell. On the other hand, asymmetry is actually a much

desired attribute for optical cell rotation, because as the optical tweezers trap either side of the cell, denser areas of the cell, or the regions where there are many structures (i.e. interfaces for refraction) will be more strongly attracted by the traps. This causes the cell to self-align with the tweezers (Perney et al. 2012). The more asymmetric the cell, the stronger the tendency to self-align, and the easier the optical traps are able to fix themselves at a specific site within the cell and rotate it as they move. Unfortunately, K-562 cells are usually spherical in suspension, and density distribution is quite uniform when healthy, therefore the traps will have to rely more on other easily controllable parameters. Some parameters that should be taken into account during cell rotation are listed in Table 2. They are categorized by stage of hologram generation at which they are taken into consideration:

Table 2. Parameters for optical cell rotation

Blazed grating	Fresnel grating	Random Binary Mask	AVI generation
- Ratio of distance between trap and the edge of the cell to the radius of the cell - Type of ramp applied on the grating	- Maximum focal depth the trap travels relative to the diameter of the cell - Wavenumber	- Block size	- Frame rate - Number of frames (between focal plane and focal length of Fresnel grating) - Axial pathway of optical traps

5.4 Results

This section selects and summarizes the final methods and parameters chosen, as well as the results for the optimization of the system.

5.4.1 Blazed Gratings

Of the three methods proposed in Chapter 4, the traditional blazed grating showed the highest efficiency in the diversion of power from the zero order to the traps at the first order. Each of the holograms was 1080 x 1080 pixels centered on the SLM display panel. Figure 29 shows the results for the traditional blazed grating. In this image, the first order (m = +1) clearly has a higher intensity than the zero order. A similar effect is observed for the multilevel grating in Figure 31. Figure 30 shows the results for the ramped blazed grating. The ramped grating has close to no effect on the zero order, while the traditional blazed grating showed the highest amount of intensity diverted from the zero order to the first order. The proportion of power directed to the first order was measured by intercepting the beam at the first lens of the telescope with a beam profiler. An image if formed here due to the Fourier transformation of the first lens. The intensity profile of this image is shown in Figure 32. Efficiency of the gratings was determined per the efficiency equation:

$$\%\ Absolute\ Efficiency = \frac{energy\ out}{energy\ in} \times 100$$

Approximately 70% of the zero order was transferred over to the first order, while that of the multilevel grating only converted about 60%.

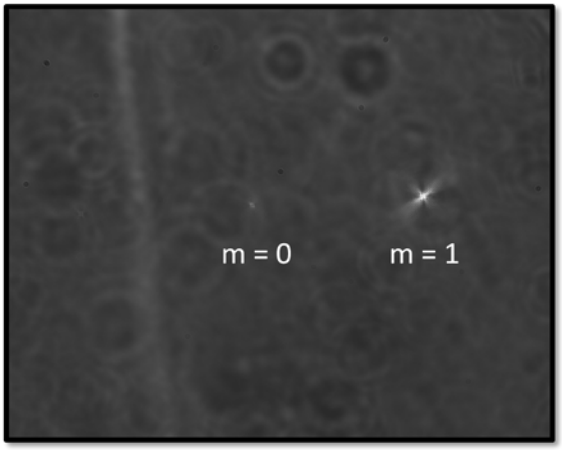

Figure 29. Optical trap generated with traditional blazed grating at m = +1

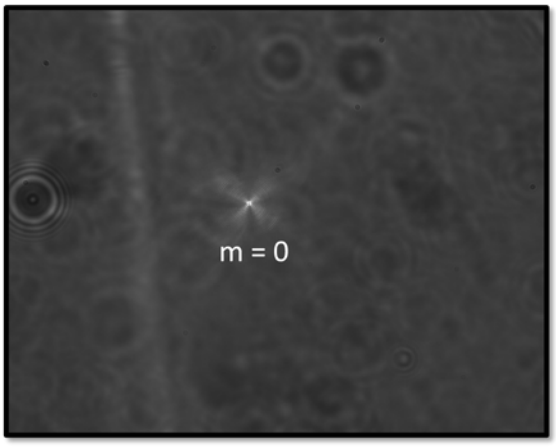

Figure 30. Optical trap generated with ramped grating

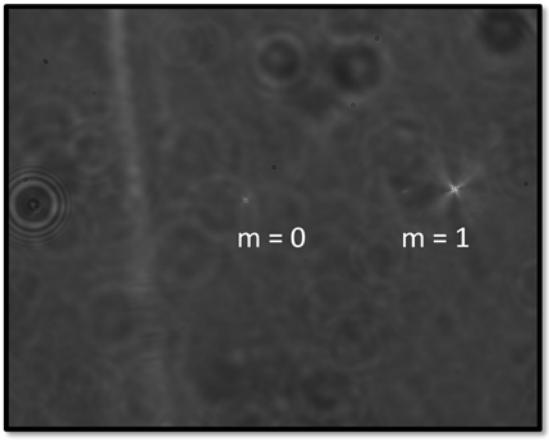

Figure 31. Optical trap generated with multilevel grating

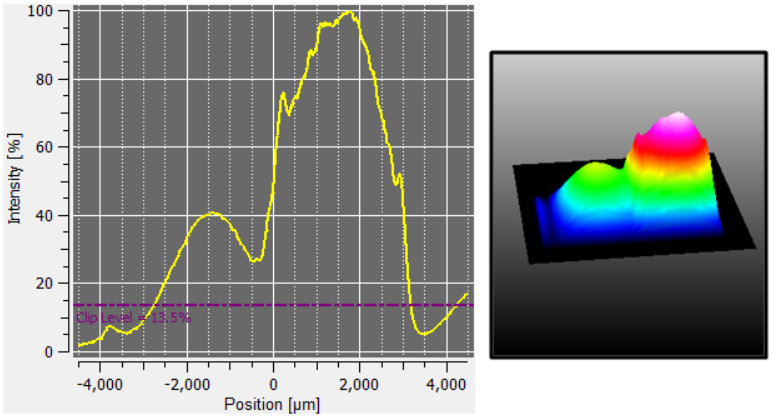

Figure 32. Beam profile of first order generated by traditional blazed grating

5.4.2 Axial Pathway

Before testing cell rotation parameters, the better method of cell rotation must first be selected. Two different rotation methods were proposed in Chapter 3. The first cell rotation method uses the torque generated by dynamic axial displacement of the two traps; the second cell rotation method uses optical tweezers to trace the circumference of the cell in a circular pattern axially. Both methods were tested and evaluated for stability of cell rotation under the same conditions and parameters. Five different live cells, all of which were different in diameter and shape, were selected for rotation. Each cell was subjected to testing for both methods. The sequence of rotation method used was randomized from cell to cell to eliminate the possibility of dependence on the previous rotation method. The parameters of the hologram generated were held constant for both methods for each cell. These parameters include frame rate, number of frames per iteration, ratio of the maximum distance between the two traps on the focal plane to the diameter of the cell, and the maximum focal length of the Fresnel gratings. The number of revolutions per minute was counted for each set of test. Results are as presented in Table 3.

Table 3. Results for comparison between cell rotation method 1 and 2

			Method 1	Method 2
Cell 1 (D=20μm)	Frame rate	16 fps	0	2
	# of frames	125		
	d:D	0.65		
	$f_{Fresnel}$	10μm		
Cell 2 (D=22μm)	Frame rate	14 fps	0	2
	# of frames	125		
	d:D	0.75		
	$f_{Fresnel}$	11μm		
Cell 3 (D=24μm)	Frame rate	12 fps	0	1
	# of frames	125		
	d:D	0.65		
	$f_{Fresnel}$	12μm		
Cell 4 (D=20μm)	Frame rate	14 fps	0	2
	# of frames	125		
	d:D	0.75		
	$f_{Fresnel}$	10μm		

The results show that the second cell rotation method is far more effective than the first. None of the cells in the first method show a full 360 degrees rotation. This may be because the final frame in the cycle does not form a continuous transition with the first frame in the next cycle. In other words, the tweezers do not trap the cell at the same

position during transition, so the cell will be free to reorient itself to the new position of the traps. The first method of rotation was therefore abandoned, and the characterization and optimization of parameters were all conducted under the second method of rotation.

5.4.3 Power

The most easily controlled and direct method of increasing stability of rotation would be by adjusting the power applied to the traps. Although the laser has a maximum output of 4W, it is inevitable that the laser beam will suffer considerable attenuation. This power loss is largely due to the diffractive nature of the SLM, but small amounts of power loss are also experienced throughout the entire optical path. It is important to characterize the attenuation of power through the optical elements, so the actual amount of power that reaches the traps can be estimated. The power loss through the optical track prior reaching the SLM is measured to be about 50%. The same efficiency equation from the previous section can be applied:

$$\%\ Absolute\ Efficiency = \frac{energy\ out}{energy\ in} \times 100$$

The power attenuation that results from the diffraction from the SLM was characterized by measuring the power of the beam before and after the SLM. Three sets if data was measured, and the average was taken. Results are listed in Table 4.

Table 4. Results for Power loss measurement on SLM samples of the beam power at different power levels

Power in (W)	Power out (W)	Efficiency (%)
1.625	0.942	57.96923
1.737	1.038	59.7582
0.2246	0.1245	55.43188

The resultant optical traps will on average only inherit a little more than 50% power from the incoming beam. From a previous section, we also know that the efficiency of the blazed grating was about 70%. The fraction of power per trap can be computed using the above information:

$$P_{per\ trap} = \frac{1}{2} \cdot P_{in} \cdot 50\% \cdot 50\% \cdot 70\%$$

The power input level used throughout the proceeding experiments in the thesis was at 4.3W. This results in having 455mW per trap. There is close to a total of 80% attenuation throughout the whole optical system from the laser to the cell.

5.4.4 Angular Resolution

The angular resolution is the angular displacement between one frame and the next. This is governed by the number of frames generated per half a rotation cycle (since each trap only travels 180 degrees). The larger the number of frames, the smaller the angle in between frames, the higher the angular resolution of the hologram sequence. The goal of this experiment is to determine the range of resolution that creates smooth cell rotation. The resolution and the pitch size of the pixels of the SLM must be taken into

account to avoid aliasing (i.e. displacement from one frame to another is smaller than is the SLM is able to produce given the Fresnel parameters). This resolution and pitch size factor will determine the maximum angular resolution, or number of frames per half revolution. This can be done analytically, by calculating the lateral and axial displacement of the traps between each frame. If any of the lateral displacements is smaller than the displacement resolution of the SLM, then aliasing will occur. To avoid singularity, where the two traps would overlap each other and cause interference that annihilates the effects of each other, the first frame will always start and end at an angle offset from the central vertical axis of the cell. This angle offset is set to be the same as that between frames for continuity. Knowing this, the minimum resolution (i.e. largest angle between frames, or minimum number of frames) needed to avoid aliasing can be calculated as follows:

From section 3.2.1

$$x_{lateral} = x_{SLM} \times M$$

where M is magnification, and was calculated to be 0.0167. In this case, x_{SLM} is equivalent to the pitch size of the SLM, which is 8μm wide. As a result, the minimum displacement allowed on the lateral plane of the image is:

$$x_{lateral} = 8 \times 0.0167 = 0.1336\ \mu m$$

The minimum angle at which the traps should travel from one frame to the other can thus be calculated using simple trigonometric relationships. The smallest lateral displacement will always be found when the trap is intersecting the 90º or 270º axes. If the displacement there is restricted to be $x_{lateral}$ = 0.1336μm, then the minimum angle is computed as follows:

$$\cos(90 - \theta_{min}) = \frac{\Delta x}{R}$$

where R is the radius of the cell, and Δx is the minimum displacement, $x_{lateral}$, then:

$$\theta_{min} = 90° - \cos^{-1}\frac{\Delta x}{R} = 0.765°$$

From the above calculations, we see that to completely eliminate aliasing, a minimum degree offset of 0.765º can be applied between each frame. This would give a maximum total of 180º/0.765º ≈ 235 frames. This level of resolution is more than enough to generate smooth trapping motions.

The coarsest level of resolution was determined experimentally. Three cells with diameters of about 20μm were selected for this experiment. The laser was set to a constant power of 4.3W (index 9.0). The overall constant traveling velocity of the traps was maintained throughout the experiment. A series of holographic videos with number of frames starting from 50 frames to 250 frames in 25 frame increments was generated and tested. As expected, the lesser the number of frames, the less stable the rotation becomes. On the other hand, the videos with number of frames from 175 to 250 frames appeared to be quite jittery. This may be due to the insufficient level of performance of the graphics card installed on the current computer. Video sequences with less frames do not appear to cause any major hindrance to rotation performance, thus the videos generated were all set to consistently have 125 frames throughout the rest of the experiments.

5.4.5 Frame Rate

The oscillation frequency of the optical traps is perhaps the most vital parameter to be characterized in order to better understand the mechanism behind optical cell

rotation. The oscillation frequency is directly related to the frame rate and the number of frames per cycle. Since the optimal range for number of frames per half revolution has already been determined in the previous section, the frequency of rotation can be calculated as follows:

$$frequency = \frac{frame\ rate\ (fps)}{number\ of\ frames}$$

The oscillation frequencies at which the cells would rotate optimally depends on the individual cell. Cells of approximately the same diameter may not necessarily share the same optimum frame rate. The optimum frame rate can be determined experimentally. Three cells that are approximately 20μm in diameter were selected, and were each subjected to rotation frame rates starting from 3 fps to 25 fps. The stability of rotation for all three cells peaked at approximately between 13 fps to 18 fps. At the lower frame rates, the cells would first snap into position, and when the traps have traveled far enough from that original position, instead of following the path of the traps, the cells will snap into their new position. The rotation of the cells was therefore discrete and discontinuous. At higher frame rates, the traps are unable to anchor the cells strongly enough to overcome the increased shear force experienced by the cell, thus the traps slip out of their initial trapping position and the cell drifts.

5.4.6 Distance to Cell Diameter Ratio

The position between the traps from the edge of the cell is also an important factor that should be taken into account. An experiment was conducted to determine the optimum ratio of the distance between the traps to the diameter of the cell. For cells of the same type and under the same conditions, it is assumed that the distribution of

densities within the cells will be similar from one cell to the other. Ideally, the traps would be generated in a region of the cell where concentration of organelles is the highest. This is because there is more change in refractive index on the light path, which would result in stronger gradient forces, resulting in stronger and more stable traps. To easily visualize the effect of trapping distance to the rotation of the cell, the experiment was conducted by laterally rotating cells with traps that were 1μm apart spanning to 25μm apart. This was done by generating a video sequence that slowly expands the radius of the rotation sequence from 1μm to 25μm, while watching the response of the cell to the revolving traps. Once the cell has reached stable rotation, the distance between the foci at that instant is recorded, and the ratio to the measured diameter of the cell is calculated. Three cells were selected for this experiment, each with a diameter of approximately 20μm. It is observed that the cells rotate best when the traps are about 13μm to 16μm apart. When the traps are too closely positioned, the cell rotates slowly, but does not seem to rotate at the same speed as that of the traps. When the traps are too far apart, the cell is not stiffly trapped, and only drifts slightly, but does not rotate at the same speed as the traps. It is observed that the cells show the most stable rotation between 13μm to 16μm, where the speed of cell rotation is roughly the same as that of the traps, and it shows stiff trapping of the cell.

5.5 Discussion

This chapter provides a detailed description of all the practical procedures and experiments that had been conducted for this thesis, and discusses results respectively. The characterization curve of the laser was provided, and the parameters of interest were briefly introduced and discussed. The chapter then moves on to present experimental

findings with regards to the parameters of interest. It is known that traditional blazed grating holograms are able to divert 70% power from the zero order to the first order, and these gratings were used throughout the experimental process. It is discovered that the method of rotation where the traps trace the circumference of the cell in a circular pattern can rotate the cell in a more stable manner than can the alternative method, where the traps travel in a vertical motion path. The reason the vertical motion of the traps were not able to rotate cells may be because the rotation relies on trapping organelles in the cell. The displacement of the traps out of the cell means that the organelles are only trapped briefly before the cell is left to drift freely. Subjecting the cells at higher frame rates (approximately 50 fps – 60 fps) only increases the frequency of oscillation or jittering of the cell, but does not necessarily induce rotation. On the other hand, the method with the circular motion trapping is able to rotate cells much more effectively. This is perhaps because of the fact that the organelles in the cells are being trapped continuously as the cell is being rotated, while it was not the case in the other method. The power at each optical trap was also estimated. After taking into account the power efficiency of the optical elements, the SLM and the blazed grating, the power efficiency of the system was estimated to be approximately 20%. The relationship between rotation quality and angular resolution, or in other words the number of frames per half cycle, was characterized. For optimal cell rotation performance, the number of frames per half cycle was measured to be within the range of 125 frames to 235 frames. This is to reduce aliasing to the minimum, and increase rotation smoothness and trapping stiffness. For convenience, the number of frames generated for each hologram video sequence was set at a constant 125 frames per half revolution. For stable rotation, the optimal oscillation

frequency was determined to be between 12 fps to 18 fps. For cells of about 20μm, the optimal distance to maintain between traps is about 13μm to 16μm.

Understandably, there may be concerns regarding the biocompatibility of lasers with cell function. These concerns are not unwarranted; numerous publications have observed localized heating at the optically trapped areas of mammalian cells (Liu et al. 1995), and is proven to cause photo damage in bacterial cells such as E. coli (Neuman et al. 1999). The aim of live cell CT is to image cells that are as close to their physiological state as possible, therefore it is important to makes sure that the method of cell rotation has minimum to no effect on the cell. The fact that a laser may cause damage to the cell while imaging is a major concern. Fortunately, the problem of photo damage at the power levels of 450mW, as is in the case of this project, has been shown to have little to no effect on mammalian cells (Barroso Peña et al. 2012). In Barroso Peña et al.'s study, holographic phase contrast microscopy was used to characterize the amount of photo damage sustained by the cell. The laser specifications used by Barroso Peña et al., such as the power level and the optical density of the tweezers, were very similar and comparable to those used in this thesis. In this aforementioned photo damage study, after being continuously exposed to a single optical trap at about 450mW over 20 minutes, the cell begins to show signs of alteration from its resting state. On the other hand, once the laser source is removed, the cell quickly recovers within 10 minutes, and returns to its original resting state. This shows that any photo damage induced by the laser levels in this optical cell rotation study is inconsequential and reversible. No doubt, the amount of literature on photo damage is still quite limited. At the current stage, cells show no notable signs of damage of change during experiments, but photo damage will be investigated nonetheless

during the 3D imaging stage, where changes in minute details in the cells can be a better indication of photo damage.

Chapter 6 Conclusion and Future Prospects

This thesis has introduced a method to orient and rotate mammalian cells in three dimensions using a phase-only spatial light modulator. The goal of this project was to adopt it into a single live-cell computed tomography platform. Although single-mammalian cell optical rotation on the perpendicular axis of the optical axis has been successfully demonstrated, the stability of this rotation is far from perfect. Ideally, the cell of interest would rotate continuously at a constant speed at about 1 rotation per minute, free of jittering or drifting. At the current stage of development, there is observable lateral drift of the cell during rotation, and depending on the speed of rotation, the cell may also go in and out of focus. This causes images to blur while taking projections, and is fatal for downstream 3D reconstruction processing.

Much continued work is needed to characterize the relationship between rotation stability and physical properties of the cell of interest. There are potentially many more motion patterns that can surpass the performance of the current method of rotation. Since the SLM can generate optical tweezers to follow virtually any imaginable motion pattern, there is great potential for improving the current method of rotation of the cell. Generating holographic patterns and characterizing them experimentally can become taxing as the amount of motion pattern options increases. COMSOL Mutiphysics, computer-aided design (CAD) modeling software, can be a useful tool to help predict the performance of the pattern before producing results experimentally. This preliminary concept filtering with COMSOL allows the best candidates to move forward for testing, increasing time and resource efficiency.

Once a specific method of rotation has been selected to be the best rotation method, the study can move forward with implementing rotation on the live cell CT platform. First, a micro-fabricated chip must be designed, so that there may be reservoirs or compartments in which to keep individual cells post-imaging. This way, the imaged cells can be extracted for further analysis or manipulation, and if so desired, imaged again. Reconstructed images will help give insight to better improve the quality of rotation. It will also shed light on potential photo damage caused by the laser, and give information on how to improve in maintaining cell vitality.

REFERENCES

Ashcroft, Brian, Vivek Nandakumar, Laimonas Kelbauskas, Honor Glenn, Roger Johnson, and Deirdre Meldrum. 2011. “Predicting 3D Nuclear Architecture Patterns in Cancer.” In *The Sixth Q-bio Conference*.

Ashkin, A. 1970. “Acceleration and Trapping of Particles by Radiation Pressure.” *Physical Review Letters* 24 (4): 156–159.

Ashkin, A, J M Dziedzic, J E Bjorkholm, and Steven Chu. 1986. “Observation of a Single-beam Gradient-force Optical Trap for Dielectric Particles.” *Optics Letters* 11 (5) (June 1): 288–290. http://www.ncbi.nlm.nih.gov/pubmed/18185672.

Banerjee, Ashis Gopal, Sagar Chowdhury, Wolfgang Losert, and Satyandra K Gupta. 2011. “Survey on Indirect Optical Manipulation of Cells, Nucleic Acids, and Motor Proteins.” *Journal of Biomedical Optics* 16 (5) (May): 051302. doi:10.1117/1.3579200. http://www.ncbi.nlm.nih.gov/pubmed/21639562.

Barroso Peña, Álvaro, Björn Kemper, Mike Woerdemann, Angelika Vollmer, Steffi Ketelhut, Gert von Bally, and Cornelia Denz. 2012. “Optical Tweezers Induced Photodamage in Living Cells Quantified with Digital Holographic Phase Microscopy.” Edited by Jürgen Popp, Wolfgang Drexler, Valery V. Tuchin, and Dennis L. Matthews. *Biophotonics* 8427 (May) (June 1): 84270A–84270A–7. doi:10.1117/12.922456. http://proceedings.spiedigitallibrary.org/proceeding.aspx?articleid=1219814.

Breidne, M, S Johansson, L-E Nilsson, and H Åhlèn. 1979. “Blazed Holographic Gratings.” *Optica Acta* 26 (11): 1427–1441.

Bronk, Burt V, Willem P Van De Merwe, and Marc Stanley. 1992. “In Vivo Measure of Average Bacterial Cell Size from a Polarized Light Scattering Function.” *Cytometry* 13: 155–162.

Carcolé, E, J Campos, and S Bosch. 1994. “Diffraction Theory of Fresnel Lenses Encoded in Low-resolution Devices.” *Applied Optics* 33 (2) (January 10): 162–74. http://www.ncbi.nlm.nih.gov/pubmed/20862004.

Carmon, G, and M Feingold. 2011. “Rotation of Single Bacterial Cells Relative to the Optical Axis Using Optical Tweezers.” *Optics Letters* 36 (1) (January 1): 40–2. http://www.ncbi.nlm.nih.gov/pubmed/21209680.

Chu, Steven, J E Bjorkholm, A Ashkin, and A Cable. 1986. “Experimental Observation of Optically Trapped Atoms.” *Physical Review Letters* 57 (3): 314–317.

Čižmár, T., O. Brzobohatý, K. Dholakia, and P. Zemánek. 2011. "The Holographic Optical Micro-manipulation System Based on Counter-propagating Beams." *Laser Physics Letters* 8 (1) (January 4): 50–56. doi:10.1002/lapl.201010100. http://doi.wiley.com/10.1002/lapl.201010100.

Dasgupta, Raktim, Sunita Ahlawat, Ravi Shankar Verma, and Pradeep Kumar Gupta. 2011. "Optical Orientation and Rotation of Trapped Red Blood Cells with Laguerre-Gaussian Mode." *Optics Express* 19 (8) (April 11): 7680–8. http://www.ncbi.nlm.nih.gov/pubmed/21503077.

Davis, J a, and D M Cottrell. 1994. "Random Mask Encoding of Multiplexed Phase-only and Binary Phase-only Filters." *Optics Letters* 19 (7) (April 1): 496–8. http://www.ncbi.nlm.nih.gov/pubmed/19844352.

EINST Technology Pte Ltd. 2003. "Brief Basic of Optical Tweezers."

Engström, David, Anders Frank, Jan Backsten, Mattias Goksör, and Jörgen Bengtsson. 2009. "Rapid SLM Design for Grid-free Multispot Positioning in 2D and 3D with a Modified Gerchberg-Saxton Algorithm." *Advances in Imaging* 1 (c): DWB13. doi:10.1364/DH.2009.DWB13. http://www.opticsinfobase.org/abstract.cfm?URI=DH-2009-DWB13.

Fauver, Mark, Eric Seibel, J Richard Rahn, Michael Meyer, Florence Patten, Thomas Neumann, and Alan Nelson. 2005. "Three-dimensional Imaging of Single Isolated Cell Nuclei Using Optical Projection Tomography." *Optics Express* 13 (11) (May 30): 4210–23. http://www.ncbi.nlm.nih.gov/pubmed/19495335.

Fuhr, G, W M Arnold, R Hagedorn, T Müller, W Benecke, B Wagner, and U Zimmermann. 1992. "Levitation, Holding, and Rotation of Cells Within Traps Made by High-frequency Fields." *Biochimica et Biophysica Acta* 1108 (2) (July 27): 215–23. http://www.ncbi.nlm.nih.gov/pubmed/1637846.

Gray, Darren S., John L. Tan, Joel Voldman, and Christopher S. Chen. 2004. "Dielectrophoretic Registration of Living Cells to a Microelectrode Array." *Biosensors and Bioelectronics* 19 (12) (July): 1765–1774. doi:10.1016/j.bios.2004.03.016. http://linkinghub.elsevier.com/retrieve/pii/S0956566304001435.

Gregory, T R. 2000. "Nucleotypic Effects Without Nuclei: Genome Size and Erythrocyte Size in Mammals." *Genome / National Research Council Canada = Génome / Conseil National de Recherches Canada* 43 (5) (October): 895–901. http://www.ncbi.nlm.nih.gov/pubmed/11081981.

Griot, Melles. 2011. "Fundamental Optics."

Herd, R M, J S Dover, and K a Arndt. 1997. “Basic Laser Principles.” *Dermatologic Clinics* 15 (3) (July): 355–72. http://www.ncbi.nlm.nih.gov/pubmed/23316665.

Hesseling, Christina, Mike Woerdemann, Andreas Hermerschmidt, and Cornelia Denz. 2011. “Controlling Ghost Traps in Holographic Optical Tweezers.” *Optics Letters* 36 (18) (September 15): 3657–9. http://www.ncbi.nlm.nih.gov/pubmed/21931423.

Hossack, Will. 2012. “Spatial Light Modulators and Modern Optical Systems”. Edinburgh. http://www2.ph.ed.ac.uk/~wjh/teaching/mo/slides/slms/slm.pdf.

Kreysing, Moritz K, Tobias Kießling, Anatol Fritsch, Jochen R Guck, A K Josef, Carl Zeiss, and Microimaging Gmbh. 2008. “The Optical Cell Rotator.” *Optics Express* 16 (21): 912–914.

Le Saux, B, B Chalmond, Y Yu, A Trouvé, O Renaud, and S L Shorte. 2009. “Isotropic High-resolution Three-dimensional Confocal Micro-rotation Imaging for Non-adherent Living Cells.” *Journal of Microscopy* 233 (3) (March): 404–16. doi:10.1111/j.1365-2818.2009.03128.x. http://www.ncbi.nlm.nih.gov/pubmed/19250461.

Leach, Jonathan, Kurt Wulff, Gavin Sinclair, Pamela Jordan, Johannes Courtial, Laura Thomson, Graham Gibson, et al. 2006. “Interactive Approach to Optical Tweezers Control.” *Applied Optics* 45 (5) (February 10): 897–903. http://www.ncbi.nlm.nih.gov/pubmed/16512531.

Leung, Clement, Zhe Lu, Xuping P Zhang, and Yu Sun. 2012. “Three-dimensional Rotation of Mouse Embryos.” *IEEE Transactions on Bio-medical Engineering* 59 (4) (April): 1049–56. doi:10.1109/TBME.2012.2182995. http://www.ncbi.nlm.nih.gov/pubmed/22231670.

Lidstrom, Mary E, and Deirdre R Meldrum. 2003. “Life-on-a-chip.” *Nature Reviews Microbiology* 1 (2) (November): 158–64. doi:10.1038/nrmicro755. http://www.ncbi.nlm.nih.gov/pubmed/15035045.

Liu, Y, D K Cheng, G J Sonek, M W Berns, C F Chapman, and B J Tromberg. 1995. “Evidence for Localized Cell Heating Induced by Infrared Optical Tweezers.” *Biophysical Journal* 68 (5) (May): 2137–44. doi:10.1016/S0006-3495(95)80396-6. http://www.pubmedcentral.nih.gov/articlerender.fcgi?artid=1282119&tool=pmcentrez&rendertype=abstract.

Miyamoto, Kenro. 1961. “The Phase Fresnel Lens.” *Journal of the Optical Society of America* 51 (1): 17–20.

Mohanty, S.K., R. Dasgupta, and P.K. Gupta. 2005. “Three-dimensional Orientation of Microscopic Objects Using Combined Elliptical and Point Optical Tweezers.”

Applied Physics B 81 (8) (November 1): 1063–1066. doi:10.1007/s00340-005-1970-7. http://link.springer.com/10.1007/s00340-005-1970-7.

Montes-Usategui, Mario, Encarnación Pleguezuelos, Jordi Andilla, and Estela Martín-Badosa. 2006. "Fast Generation of Holographic Optical Tweezers by Random Mask Encoding of Fourier Components." *Optics Express* 14 (6) (March 20): 2101–2107. http://www.ncbi.nlm.nih.gov/pubmed/19503542.

Nandakumar, Vivek, Xing An, Yalin Wang, Roger Johnson, and Deirdre Meldrum. 2012. "Conformal Mapping of Nuclei in 3D Tomographic Cell Images to Assess Shape Herterogeneity." In *2012 9th IEEE International Symposium on Biomedical Imaging*, 222–225. Barcelona, Spain.

Nandakumar, Vivek, Mark R. Holl, and Deirdre R. Meldrum. 2008. "A Flexible Framework for Automation of Single Cell and Cell-to-cell Interaction Analyses." In *2008 4th IEEE International Conference on Automation Science and Engineering*, 424–430. Washington DC, USA: Ieee. doi:10.1109/COASE.2008.4626576. http://ieeexplore.ieee.org/lpdocs/epic03/wrapper.htm?arnumber=4626576.

Nandakumar, Vivek, Laimonas Kelbauskas, Roger Johnson, and Deirdre Meldrum. 2011. "Quantitative Characterization of Preneoplastic Progression Using Single-cell Computed Tomography and Three-dimensional Karyometry." *Cytometry. Part A : the Journal of the International Society for Analytical Cytology* 79 (1) (January): 25–34. doi:10.1002/cyto.a.20997. http://www.pubmedcentral.nih.gov/articlerender.fcgi?artid=3068856&tool=pmcentrez&rendertype=abstract.

Neuman, Keir C., Edmund H. Chadd, Grace F. Liou, Keren Bergman, and Steven M. Block. 1999. "Characterization of Photodamage to Escherichia Coli in Optical Traps." *Biophysical Journal* 77 (5) (November): 2856–2863. doi:10.1016/S0006-3495(99)77117-1. http://linkinghub.elsevier.com/retrieve/pii/S0006349599771171.

Parkin, Simon, Gregor Knöner, Wolfgang Singer, Timo a Nieminen, Norman R Heckenberg, and Halina Rubinsztein-Dunlop. 2007. "Optical Torque on Microscopic Objects." *Methods in Cell Biology*. doi:10.1016/S0091-679X(06)82019-4. http://www.ncbi.nlm.nih.gov/pubmed/17586271.

Perney, Nicolas M B, Peter Horak, Neil a Hanley, and Tracy Melvin. 2012. "The Self-orientation of Mammalian Cells in Optical Tweezers-the Importance of the Nucleus." *Physical Biology* 9 (2) (January): 024001. doi:10.1088/1478-3975/9/2/024001. http://www.ncbi.nlm.nih.gov/pubmed/22473086.

Rosen, Joseph, Barak Katz, Gary Brooker, and P O Box. 2009. "Review of Three-dimensional Holographic Imaging by Fresnel Incoherent Correlation Holograms." *3D Research* 1 (1): 1–9.

Sato, S, M Ishigure, and H Inaba. 1991. “Optical Trapping and Rotational Manipulation of Microscopic Particles and Biological Cells Using Higher-order Mode Nd:YAG Laser Beams.” *Electronics Letters* 27 (20): 1831–1832.

Schnelle, Thomas, Torsten Muller, Gabriele Grandl, Stephen G. Shirley, and Gunter Fuhr. 2000. “Dielectrophoretic Manipulation of Suspended Submicron Particles.” *Electrophoresis* 21: 66–73.

Sheu, Fang-Wen, Tzu-Kai Lan, Yu-Chung Lin, Shiung Chen, and Chyung Ay. 2010. “Stable Trapping and Manually Controlled Rotation of an Asymmetric or Birefringent Microparticle Using Dual-mode Split-beam Optical Tweezers.” *Optics Express* 18 (14) (July 5): 14724–9. http://www.ncbi.nlm.nih.gov/pubmed/20639958.

Van der Horst, Astrid, Benjamin P B Downing, and Nancy R Forde. 2009. “Position and Intensity Modulations in Holographic Optical Traps Created by a Liquid Crystal Spatial Light Modulator.” *Optical Society of America* 1: 8–10. doi:10.1364/OTA.2009.OMB3.

Wang, X, D Wilson, R Muller, P Maker, and D Psaltis. 2000. “Liquid-crystal Blazed-grating Beam Deflector.” *Applied Optics* 39 (35) (December 10): 6545–55. http://www.ncbi.nlm.nih.gov/pubmed/18354668.

Zalevsky, Z, D Mendlovic, and R G Dorsch. 1996. “Gerchberg-Saxton Algorithm Applied in the Fractional Fourier or the Fresnel Domain.” *Optics Letters* 21 (12) (June 15): 842–4. http://www.ncbi.nlm.nih.gov/pubmed/19876177.

APPENDIX A

IMAGES OF OPTICAL SET-UP

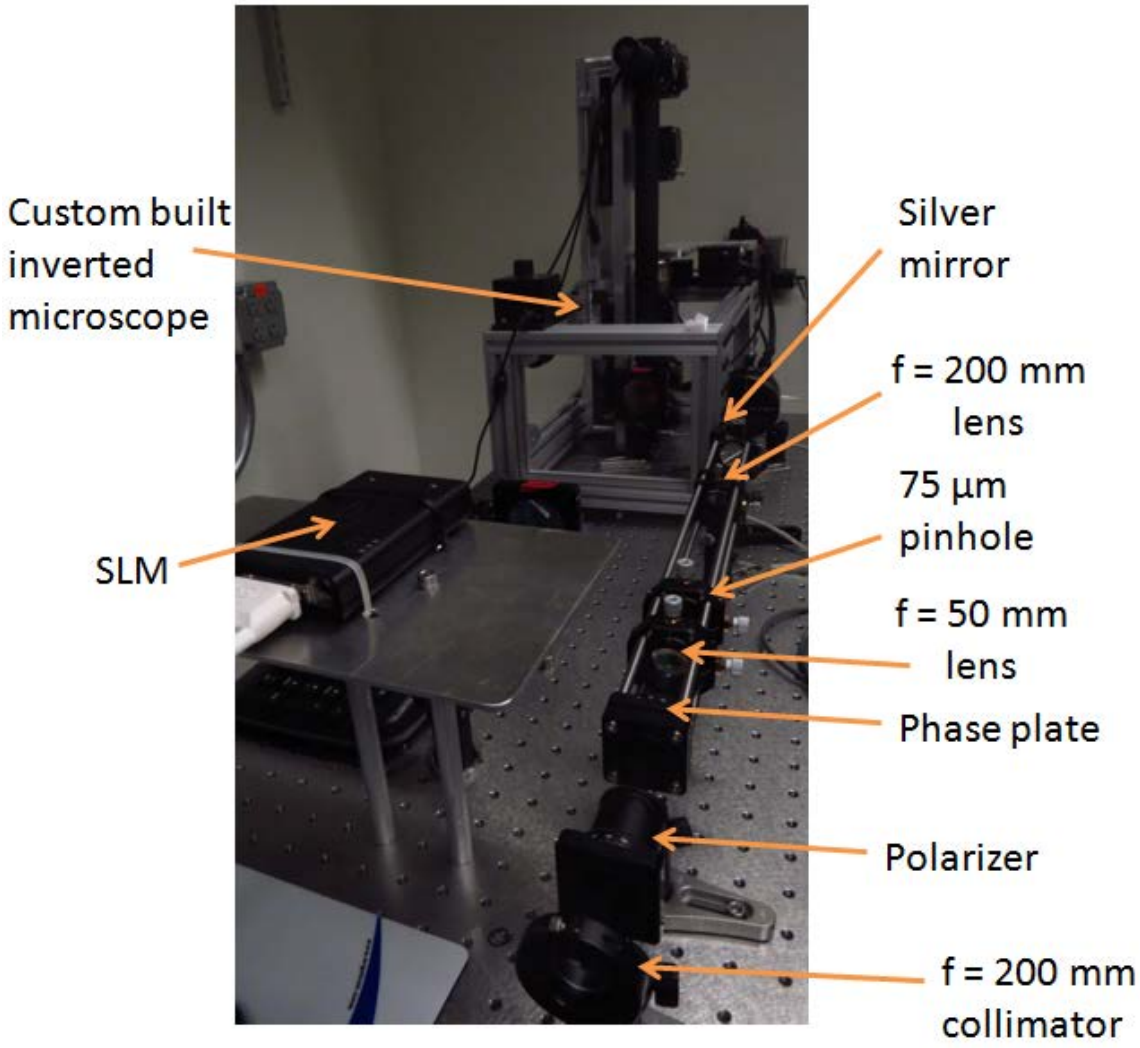

Appendix A1 Optical tweezers experimental set-up 1

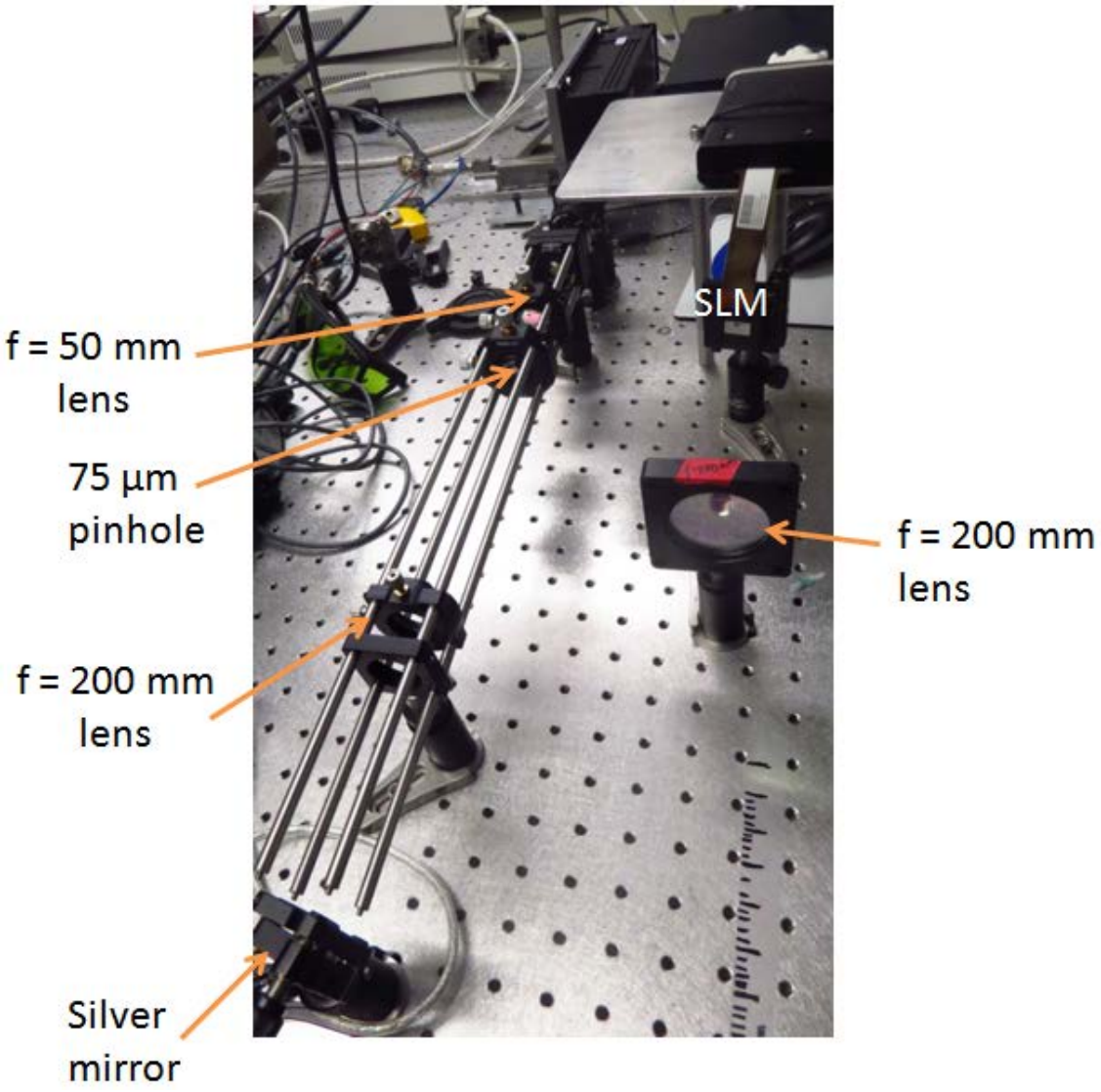

Appendix A2 Optical tweezers experimental set-up 2

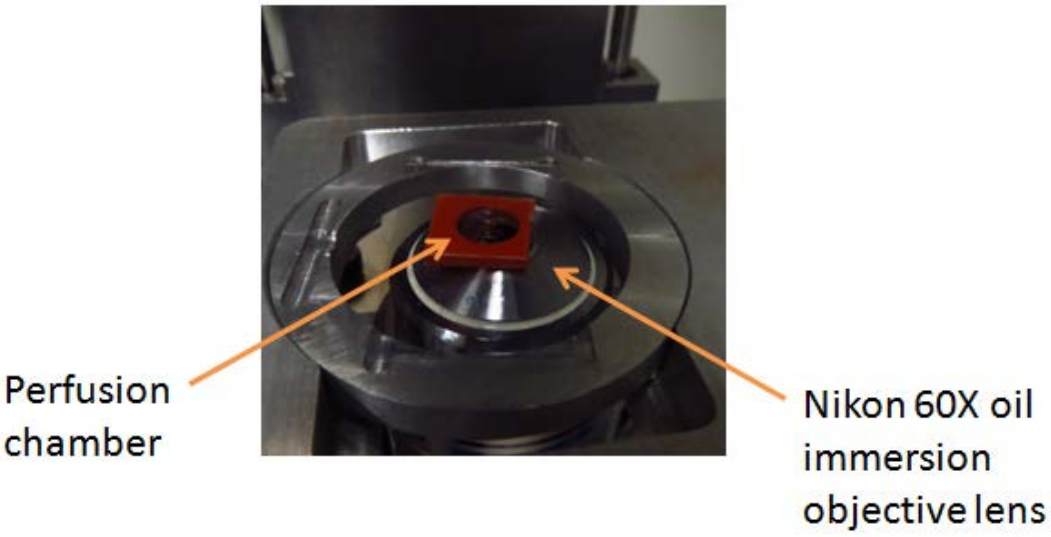

Appendix A3 Perfusion chamber attached onto microslide above objective lens